J. Fluid Mech. (2000), *vol.* 404, *pp.* 311–343. Printed in the United Kingdom

Convection-driven dynamos in a rotating plane layer

By CHRIS A. JONES AND PAUL H. ROBERTS†

School of Mathematical Sciences, University of Exeter EX4 4QE, UK

(Received 17 June 1998 and in revised form 19 October 1999)

The plane layer Childress–Soward dynamo model, consisting of a rotating layer of electrically conducting fluid between horizontal planes heated from below, is studied. Solutions periodic in the horizontal directions are sought, with electrically insulating boundary conditions applied. The large Prandtl number limit is used.

Fully three-dimensional convection-driven dynamos have been studied numerically for this problem. Both the kinematic and the magnetically saturated regimes are studied, and a simple model of the dynamo mechanism is proposed. The dependence of the dynamo on the Rayleigh number, Ekman number and diffusivity ratio is studied, and the role of Taylor's constraint in low Ekman number convection-driven dynamos is considered.

1. Introduction

Considerable progress in the understanding of the geodynamo has been made in the last few years. Numerical simulations of convection in the Earth's liquid core show some remarkable similarities with relevant geophysical data (Glatzmaier & Roberts 1995*a*; Jones, Longbottom & Hollerbach 1995). The simulations generate fields of approximately the right strength and morphology, which can undergo reversals similar to those of the geodynamo (Glatzmaier & Roberts 1995*b*), and the secular variation in the simulations broadly resembles that of the geomagnetic field.

Although the progress made in geodynamo simulations is very encouraging for the basic model, our understanding of nonlinear convection-driven dynamos is still very incomplete. In order to eliminate numerical instabilities, all the simulations referred to above have had to introduce hyperviscosity into the governing equations, and as recently pointed out by Zhang & Jones (1997) this can affect the dynamics of rapidly rotating fluids, perhaps significantly. Furthermore, none of the simulations have yet reached the very low Ekman number that obtains in the Earth's core which is $O(10^{-15})$ if laminar values of the viscosity are used, and is still $O(10^{-8})$ even if turbulent viscosity is assumed. By contrast, the numerical solutions in spherical geometry seldom have E less than 10^{-4} unless hyperviscosity is used (or very short runs performed); also, because of the very large amounts of CPU time required by a spherical dynamo code, very little exploration of parameter space has been possible. The laminar value of q, the ratio of thermal to magnetic diffusivity, is very small in the Earth, but in the numerical models q cannot be made small because then very

† Permanent address: Department of Mathematics, University of California, Los Angeles, CA 90095, USA.

large Rayleigh numbers are required for dynamo action to occur; this creates serious resolution problems.

In view of these difficulties, it is natural to look at the the plane layer model discussed here to enhance our understanding of nonlinear convection-driven dynamos. The pseudo-spectral technique has so far proved to be the most effective way of solving convection-driven dynamos in spherical geometry, and we use this method here for the plane layer problem also. The plane layer model has some significant computational advantages over the spherical geometry problem; it allows the use of fast Fourier transforms in all three spatial directions, thus allowing a fully three-dimensional simulation to be performed relatively cheaply. This is not possible in the spherical case, because no practically useful fast Legendre transform exists, so that transforming between the spherical harmonic spectral space and physical space is very slow. A further advantage of the plane layer model is that the storage required is very much less than that used by a spherical code. In consequence, exploration and understanding of the dynamical processes involved in the three-dimensional dynamo becomes a realistic possibility. Nevertheless, as we see below, there is a major difficulty with the spherical geometry dynamo that also affects the plane layer problem: as the Ekman number is reduced, the timestep has to be reduced in order to maintain numerical stability (see e.g. Walker, Barenghi & Jones 1998). This prevents us from reaching very low Ekman number.

The first investigations of the plane layer model were those of Childress & Soward (1972), Soward (1974), Fautrelle & Childress (1982), and Meneguzzi & Pouquet (1989), who established that dynamo action occurs in this problem, and that subcritical behaviour can occur. More recently, St. Pierre (1994) investigated the generation of strong fields in the plane layer model. This work builds on that of St. Pierre; however, partly because of his experience, we have made some changes to the boundary conditions on the horizontal bounding planes.

The important issues for our problem are (i) to establish the nature of convection in the absence of a magnetic field; (ii) to discover whether the convection generates a magnetic field; (iii) to investigate the mechanism by which the dynamo saturates; and (iv) to determine whether Taylor's (1963) constraint is satisfied at low Ekman number. If these issues can be answered, it should be possible to gain some insight into how the field strength and morphology vary with the input parameters.

Issue (i) is an essential pre-requisite in understanding the problem. As we shall see, the magnetic field does affect the nature of the convection somewhat when saturation is reached, but many of the basic features of the non-magnetic convection persist even at quite large field strengths. Problem (ii) is not such a simple matter as might be supposed; several times in the past flows have been proposed in the belief that they can act as dynamos, a belief that could not be unequivocally supported even after detailed investigations. Matthews (1999) has recently performed some analysis on the kinematic dynamo problem with plane layer convection, and Brandenburg *et al.* (1996) looked at the compressible convection problem. Problem (iii) has been the subject of considerable speculation, but is still very uncertain. Here we explore the parametric dependence of the saturated field strength, and discuss a simple model which may be relevant. Problem (iv) is another difficult issue: a number of nonlinear α^2-dynamo models (Soward & Jones 1983) verified the Malkus–Proctor scenario, in which the dynamo evolves into a Taylor state as it moves further into the nonlinear regime, but not all models do this (e.g. Jones & Roberts 1990). Another possibility is the development of large geostrophic flows, along the lines first suggested by Braginsky (1975) in his two-dimensional model-Z dynamos.

2. Model description and governing equations

We consider a conducting fluid layer confined between horizontal boundaries at $z = \pm\frac{1}{2}d$. We seek solutions in the form of convection cells, i.e. solutions in a 'box' that are periodic in both the x-direction (period $2\pi d/\alpha$) and the y-direction (period $2\pi d/\beta$). Most attention has been paid to the case of a cubical cell, that is $\alpha = \beta = 2\pi$. Note that this does preclude the possibility of long-wavelength fields developing; recent work on magnetoconvection (Weiss *et al.* 1996) has shown that long-wavelength fields can develop, but to follow these demands an enhanced computing requirement, so that the advantages of the plane layer model are reduced. It seems sensible at this stage to address the problem with $O(d)$ horizontal wavelengths first.

The magnetic diffusivity is η, the thermal diffusivity κ and the kinematic viscosity ν. The layer is rotating at angular velocity Ω about a vertical axis in the z-direction, and gravity g acts in the $-z$-direction. The coefficient of thermal expansion is $\bar{\alpha}$ and the temperature difference across the layer is $\bar{\beta}d$.

In the Earth's core, the inertial terms in the momentum equation are small compared with the Coriolis term (low Rossby number) and are often neglected, as in the high Prandtl number limit ($\nu/\kappa \to \infty$) considered here. Taking the high Prandtl number limit eliminates any high-frequency inertial modes from the problem. Taking the lengthscale as the layer depth d, the timescale as the magnetic diffusion time d^2/η, the magnetic field unit as $(2\Omega\rho\mu\eta)^{1/2}$ (where ρ is the fluid density and μ the permeability) and the temperature unit as $\bar{\beta}d$, the governing equations are

$$\hat{\boldsymbol{z}} \times \boldsymbol{u} = -\nabla p + \boldsymbol{j} \times \boldsymbol{B} + qRa\theta\hat{\boldsymbol{z}} + E\nabla^2\boldsymbol{u}, \tag{2.1}$$

$$\frac{\partial \boldsymbol{B}}{\partial t} = \nabla \times (\boldsymbol{u} \times \boldsymbol{B}) + \nabla^2\boldsymbol{B}, \tag{2.2}$$

$$\frac{\partial \theta}{\partial t} + \boldsymbol{u} \cdot \nabla\theta = q\nabla^2\theta + \boldsymbol{u} \cdot \hat{\boldsymbol{z}}, \tag{2.3}$$

$$\nabla \cdot \boldsymbol{B} = 0, \tag{2.4}$$

$$\nabla \cdot \boldsymbol{u} = 0, \tag{2.5}$$

where $\boldsymbol{B}$ is the magnetic field, θ is the difference between the actual temperature gradient and the static temperature gradient and $\boldsymbol{j} = \nabla \times \boldsymbol{B}$ is the current density. The three dimensionless parameters are E, the Ekman number, Ra, the Rayleigh number and q, the diffusivity ratio defined by

$$E = \frac{\nu}{2\Omega d^2}, \quad Ra = \frac{g\bar{\alpha}\bar{\beta}d^2}{2\Omega\kappa}, \quad q = \frac{\kappa}{\eta}.$$

We are here adopting the definition of Ra usual in studies of rapidly rotating fluids; the Rayleigh number more commonly employed in studies of non-rotating convection is (e.g. Chandrasekar 1961) $g\bar{\alpha}\bar{\beta}d^4/\kappa\nu = Ra/E$.

The linear theory for this plane layer problem, with no restrictions on the allowed horizontal wavelengths, has recently been further studied by Roberts & Jones (1999).

The velocity and magnetic field are expanded in toroidal and poloidal components, but in the plane layer geometry horizontally averaged horizontal components must be added explicitly to obtain the complete representation:

$$\boldsymbol{u} = \nabla \times e\hat{\boldsymbol{z}} + \nabla \times \nabla \times f\hat{\boldsymbol{z}} + U_x\hat{\boldsymbol{x}} + U_y\hat{\boldsymbol{y}}, \tag{2.6}$$

$$\boldsymbol{B} = \nabla \times g\hat{\boldsymbol{z}} + \nabla \times \nabla \times h\hat{\boldsymbol{z}} + b_x\hat{\boldsymbol{x}} + b_y\hat{\boldsymbol{y}}. \tag{2.7}$$

Here U_x and U_y define what we call 'the mean velocity', and b_x and b_y define 'the mean field'; they are functions of z and t alone.

The scalar equations solved are formed by taking the z-components of the curl and of the curl curl of equation (2.1) and the z-components of (2.2) and of the curl of (2.2):

$$\nabla_H^2 \frac{\partial f}{\partial z} + E\nabla^2\nabla_H^2 e = F_1, \tag{2.8}$$

$$\nabla_H^2 \frac{\partial e}{\partial z} - E\nabla^4\nabla_H^2 f = F_2 - qRa\nabla_H^2\theta, \tag{2.9}$$

$$\nabla_H^2 \frac{\partial h}{\partial t} - \nabla^2\nabla_H^2 h = -G_1, \tag{2.10}$$

$$\nabla_H^2 \frac{\partial g}{\partial t} - \nabla^2\nabla_H^2 g = -G_2, \tag{2.11}$$

where ∇_H^2 denotes the horizontal Laplacian, and

$$F_1 = \hat{\boldsymbol{z}} \cdot \nabla \times (\boldsymbol{j} \times \boldsymbol{B}), \qquad F_2 = \hat{\boldsymbol{z}} \cdot \nabla \times \nabla \times (\boldsymbol{j} \times \boldsymbol{B}), \tag{2.12a,b}$$

$$G_1 = \hat{\boldsymbol{z}} \cdot \nabla \times (\boldsymbol{u} \times \boldsymbol{B}), \qquad G_2 = \hat{\boldsymbol{z}} \cdot \nabla \times \nabla \times (\boldsymbol{u} \times \boldsymbol{B}). \tag{2.13a,b}$$

Our fifth scalar equation is (2.3).

These equations must be supplemented by the equations for the horizontally averaged components:

$$-U_y = E\frac{\partial^2 U_x}{\partial z^2} + \hat{\boldsymbol{x}} \cdot \langle \boldsymbol{j} \times \boldsymbol{B} \rangle, \tag{2.14}$$

$$U_x = E\frac{\partial^2 U_y}{\partial z^2} + \hat{\boldsymbol{y}} \cdot \langle \boldsymbol{j} \times \boldsymbol{B} \rangle, \tag{2.15}$$

$$\frac{\partial b_x}{\partial t} = \frac{\partial^2 b_x}{\partial z^2} + \hat{\boldsymbol{x}} \cdot \langle \nabla \times (\boldsymbol{u} \times \boldsymbol{B}) \rangle, \tag{2.16}$$

$$\frac{\partial b_y}{\partial t} = \frac{\partial^2 b_y}{\partial z^2} + \hat{\boldsymbol{y}} \cdot \langle \nabla \times (\boldsymbol{u} \times \boldsymbol{B}) \rangle, \tag{2.17}$$

where $\langle\ \rangle$ denotes the horizontal average

$$\langle f \rangle = \frac{\alpha\beta}{4\pi^2} \int f \, \mathrm{d}x \, \mathrm{d}y.$$

The choice of boundary conditions is rather important. The geodynamo simulations suggest that the Ekman layers can play an important role in the dynamo process, so we have adopted no-slip velocity boundary conditions,

$$e = f = \frac{\partial f}{\partial z} = U_x = U_y = 0 \quad \text{on } z = \pm\tfrac{1}{2}. \tag{2.18}$$

St. Pierre's solutions using perfectly conducting boundaries led to a build up of field near the boundaries, an undesirable feature from a numerical point of view. In the Earth, insulating boundary conditions are a reasonable approximation at the core–mantle boundary; the conductivity of the inner core is however a significant feature in geodynamo modelling. Here we assume that there is electrically insulating material above and below the conducting fluid layer, which avoids these numerical difficulties. The magnetic field outside the fluid layer is then current-free; using (2.7), $j_z = 0$

implies $g = 0$ in the insulators, and $j_x = j_y = 0$ implies $\nabla^2 h = 0$ there. Zero current in the insulators implies that the mean field there, $(b_x, b_y, 0)$, must be constant in z. We could take this constant to be non-zero, but this would correspond to the problem of dynamo action in an imposed external field, which we do not address in this paper. We therefore assume the field tends to zero at large distance from the layer, so that in the insulators $b_x = b_y = 0$. Continuity of tangential field then requires

$$g = b_x = b_y = 0 \quad \text{on } z = \pm\tfrac{1}{2}, \tag{2.19}$$

and since each component of the potential field h must decay exponentially away from the layer, continuity of h and its vertical derivative implies that

$$\frac{\partial h_{lm}}{\partial z} = \mp a\, h_{lm} \quad \text{on } z = \pm\tfrac{1}{2}, \tag{2.20}$$

where h_{lm} denotes the Fourier component of h with wavenumber $l\alpha$ in the x-direction and $m\beta$ in the y-direction, and which therefore has a total wavenumber of $a = (l^2\alpha^2 + m^2\beta^2)^{1/2}$. The temperature condition is

$$\theta = 0 \quad \text{on } z = \pm\tfrac{1}{2}. \tag{2.21}$$

The equations are solved by the pseudo-spectral method, a brief description being given in the Appendix. The fields are expanded in Fourier series in x and y, and Chebyshev series in z. The Fourier series are truncated at the N_x and N_y levels, so only harmonics in the range $(-N_x, N_x)$ and $(-N_y, N_y)$ are retained, and N_z Chebyshev components are retained. We have not imposed any particular symmetry on the solutions; because of the Boussinesq symmetry and the periodic boundary conditions many symmetric solutions exist. In choosing the initial conditions, care must be taken to make sure that a complete set is selected. This was done by giving each temperature and magnetic field component in the spectral expansion a small random value. Note that because the inertial terms are ignored, initial values are not required for the velocity perturbations.

As we shall see below, the mean components of the magnetic field, b_x and b_y, play an important role in the dynamo process. If we integrate the x-component of the induction equation over the plane area $x =$ constant, $0 \leqslant y \leqslant 2\pi/\beta$, $-\frac{1}{2} \leqslant z \leqslant \frac{1}{2}$, the surface integral of $\nabla \times (\boldsymbol{u} \times \boldsymbol{B})$ vanishes, because $\boldsymbol{u}$ vanishes on the horizontal boundaries, and the contributions at $y = 0$ and $y = 2\pi/\beta$ cancel by the periodicity condition. It follows that

$$\frac{\partial}{\partial t}\int_S (\hat{\boldsymbol{x}} \cdot \boldsymbol{B})\, \mathrm{d}y\, \mathrm{d}z = -\int_C (\nabla \times \boldsymbol{B}) \cdot \mathrm{d}\boldsymbol{l}, \tag{2.22}$$

where C is the perimeter of the plane area. If we average (2.22) over x, we obtain

$$\frac{\partial}{\partial t}\int_S b_x\, \mathrm{d}z = \left.\frac{\partial b_x}{\partial z}\right|_{z=1/2} - \left.\frac{\partial b_x}{\partial z}\right|_{z=-1/2}, \tag{2.23}$$

and a similar result holds for b_y. Now if the boundaries were perfect conductors, (2.23) and its y-analogy would imply that $\bar{b}_x$ and $\bar{b}_y$, the vertical average of b_x and b_y, would be zero, i.e. no net mean field could develop. With our insulating boundary conditions, this is no longer true: a net mean field is possible. However, the mean field cannot be maintained with the same sign everywhere: if, for example, b_x were positive for all z in the interior, then the right-hand side of (2.23) would be be negative, so that $\bar{b}_x$ would decrease.

Other quantities of interest are the kinetic and magnetic energies. These can be

divided into toroidal, poloidal and mean parts. After various integrations the toroidal magnetic energy reduces to

$$\mathscr{T} = \frac{1}{2}\int (\nabla_H g)^2 \, \mathrm{d}v. \tag{2.24}$$

The poloidal magnetic energy in the layer is

$$\mathscr{P}_l = \frac{1}{2}\int \left[\left(\nabla_H \frac{\partial h}{\partial z}\right)^2 + (\nabla_H^2 h)^2\right] \mathrm{d}v, \tag{2.25}$$

and the poloidal energy outside the layer (in the vacuum region) can be written as a surface integral over, A, the two horizontal surfaces at $z = \pm\frac{1}{2}$:

$$\mathscr{P}_v = \frac{1}{2}\int_A \nabla_H h \cdot \nabla_H \frac{\partial h}{\partial z} \, \mathrm{d}S. \tag{2.26}$$

The total poloidal contribution to the magnetic energy is $\mathscr{P} = \mathscr{P}_l + \mathscr{P}_v$. The mean field contributes

$$\mathscr{M} = \frac{1}{2}\int [b_x^2 + b_y^2] \, \mathrm{d}v, \tag{2.27}$$

and the total magnetic energy is $\mathscr{E}_m = \mathscr{T} + \mathscr{P} + \mathscr{M}$.

Analogous expressions for the kinetic energy $\mathscr{E}_u = \mathscr{T} + \mathscr{P} + \mathscr{M}$, with the e, f, U_x and U_y replacing the magnetic quantities in (2.24) to (2.27) hold, except that there is no contribution from the vacuum region in this case.

It is useful to define the magnetic and kinetic energies in each l, m mode separately, which we write as $\mathscr{E}_m(l,m)$ and $\mathscr{E}_u(l,m)$ respectively. It is also convenient to introduce the root-mean-square magnetic field and velocity in each mode defined as

$$\mathscr{B}_{lm} = \sqrt{2\mathscr{E}_m(l,m)}, \quad \text{and} \quad \mathscr{U}_{lm} = \sqrt{2\mathscr{E}_u(l,m)}. \tag{2.28}$$

Important derived quantities for understanding convection-driven dynamos are the magnetic Reynolds number and the Elsasser number, which is a measure of the relative strength of the Lorentz force and the Coriolis force. Our dimensionless scaling means that dimensionless velocities can be interpreted directly as local magnetic Reynolds numbers R_m. Our scaling for the field means that the square of the dimensionless field strength is a measure of the local Elsasser number Λ. Occasionally it is convenient to have an average value of R_m for comparisons, and we adopt $\sqrt{2\mathscr{E}_u}$ for this.

3. Non-magnetic convection

Since comparisons between the working convective dynamo and the non-magnetic layer are revealing, we devote this section to the latter. The parameter q has no meaning when $\boldsymbol{B} \equiv 0$. It can be scaled out of the governing equations (2.1), (2.3) and (2.5) by the simple transformation

$$\boldsymbol{u} \to q\boldsymbol{u}, \quad p \to qp, \quad t \to t/q. \tag{3.1}$$

In figures 2 and 3 below, time is measured in units of d^2/q, which is equivalent to taking $q = 1$.

3.1. *Marginal convection*

Consider first marginal convection. Since there is no preferred horizontal direction, it suffices to consider infinitesimal disturbances with one wavenumber, α. As is well-known (e.g. Chandrasekhar 1961), in our infinite Prandtl number limit, overstability

	$E = 10^{-3}$				$E = 2 \times 10^{-4}$			
$m\backslash l$	0	1	2	3	0	1	2	3
0		95.4554	74.6686	162.3890		243.5087	149.1197	119.9983
1	95.4554	75.2682	83.8008	191.2088	243.5087	191.5763	137.6978	120.1579
2	74.6686	83.8008	137.0776	297.9538	149.1197	137.6978	121.3732	128.3037
3	162.3890	191.2088	297.9538	541.1425	119.9983	120.1579	128.3037	162.3404

TABLE 1. Critical Rayleigh numbers for modes with wavenumbers $2l\pi$ and $2m\pi$.

cannot occur, so convection onsets directly with a pitchfork bifurcation at a critical Rayleigh number Ra_c. At low Prandtl numbers, this is no longer the case (Zhang & Roberts 1997, 1998), and high-frequency inertial waves are excited. The wavenumber of the first mode to become unstable in the unbounded plane layer is denoted by α_c. This increases as $E \to 0$; in fact, $\alpha_c = O(E^{-1/3})$.

As explained above, it is not practical to study the unrestricted plane layer for computational reasons. We therefore restrict our attention to solutions 'in a box', i.e. those that are periodic in both the x- and y-directions, with wavelengths of $2\pi/\alpha$ and $2\pi/\beta$ respectively. Thus l and m are restricted to integral values, and we denote a mode of wavenumber $l\alpha$ in the x-direction and $m\beta$ in the y-direction by (l, m).

Two box sizes were considered: the cubic box with $\alpha = \beta = 2\pi$, so the box has the same wavelength as the layer depth in both x- and y-directions, and a rectangular box with $\alpha = \beta = 2\sqrt{2}\pi$, a taller thinner box. The reason for investigating the narrower box is that, as we shall see below, dynamo action onsets at a lower magnetic Reynolds number in the narrower box, so that its behaviour can be investigated more readily. It would be of interest to consider wider boxes, but unfortunately this is expensive computationally.

Table 1 shows the marginal Rayleigh number for the lowest modes (i.e. those of smallest l and m) in the case of the cubical box at $E = 10^{-3}$ (left) and at $E = 2 \times 10^{-4}$ (right).

3.2. *Finite-amplitude convection*

As suggested by the results of table 1 for the marginal case, convection at finite amplitude is dominated by long-wavelength modes though not by the longest wavelength modes: of those shown on the left-hand side of the table, the $(2, 0)$, $(0, 2)$, $(1, 1)$, $(2, 1)$ and $(1, 2)$ modes are all more easily excited than the $(1, 0)$ and $(0, 1)$ modes.

Although at $E = 10^{-3}$ the modes $(2, 0)$ and $(0, 2)$ are the first to become excited as Ra is increased, in the mildly supercritical regime they soon become less important than the $(1, 1)$ and $(1, -1)$ modes. Thus at $Ra = 95$ numerical integration of the time-dependent convection equations leads to a steady finite-amplitude state in which either the $(1, 1)$ or $(1, -1)$ mode dominates depending on the starting conditions (see figures 1*a*, *b*). If the Rayleigh number is increased, the modes $(1, 0)$ and $(0, 1)$ start to play a more significant role. At $Ra = 125$ we see the appearance of a stable heteroclinic orbit, as found in a related problem by Busse & Heikes (1980) and Soward (1984). The existence of this heteroclinic orbit depends on the symmetry of our problem about the midplane $z = 0$. The heteroclinic orbits observed by Busse & Heikes were found from the amplitude equations, but here we see that they exist even in a full numerical integration. The situation is more complex than that analysed by Busse & Heikes and by Soward, for we have four modes interacting $(1, 0)$, $(1, 1)$, $(0, 1)$ and $(1, -1)$. The pair

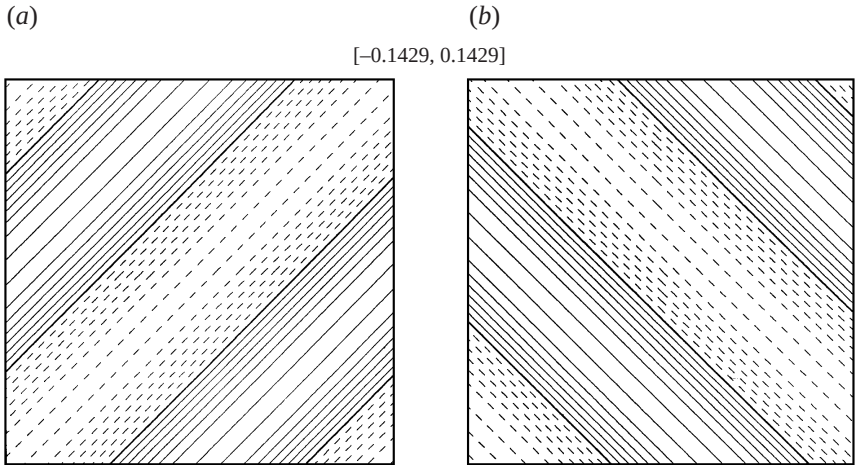

FIGURE 1. Convection without magnetic field at $Ra = 95$, $E = 0.001$ in the (x, y)-plane at $z = 0$ with $\alpha = \beta = 2\pi$. Contours of temperature at intervals of 0.02 for (*a*) the $(1, -1)$ roll, (*b*) the $(1, 1)$ roll. In this and subsequent similar figures dashed contours have negative values, the bold contour is the zero level. The values in brackets denote the minimum and maximum values attained by the contoured quantity.

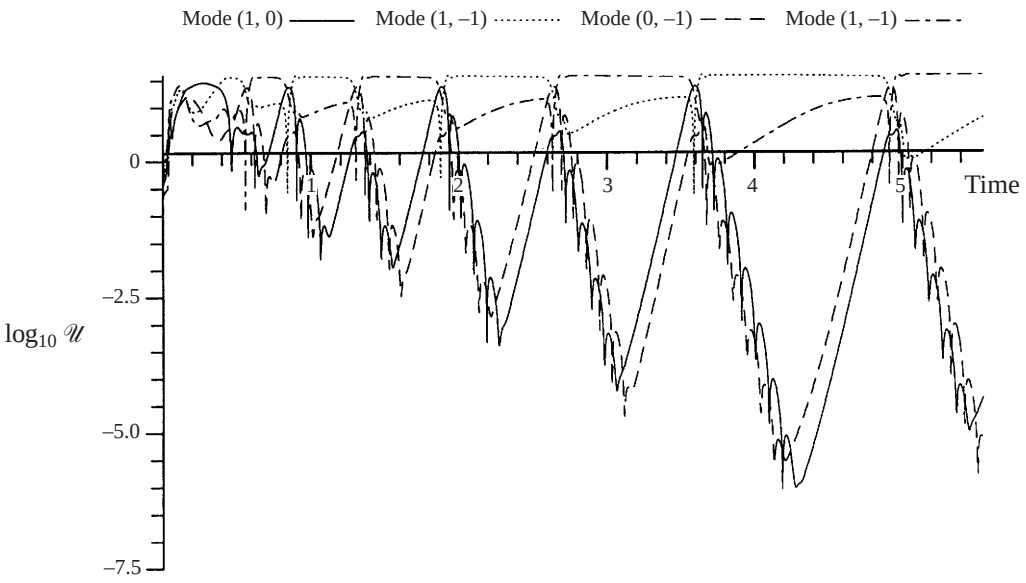

FIGURE 2. The logarithm of the root-mean-square velocity, $\log_{10} \mathscr{U}_{lm}$, of the modes $(1, 0)$, $(1, 1)$, $(0, 1)$ and $(1, -1)$, as a function of time for $Ra = 125$, $E = 0.001$, $\alpha = \beta = 2\pi$, showing the heteroclinic cycle.

$(1, 1)$ and $(1, -1)$ dominate over the other two in the sense that the trajectories spend more time in their vicinity than they do in the vicinity of $(1, 0)$ and $(0, 1)$. Nevertheless, the Küppers–Lortz instability (Küppers & Lortz 1969) is effective at $Ra = 125$, and the modes cycle round the sequence $(1, 0) \rightarrow (1, 1) \rightarrow (0, 1) \rightarrow (1, -1) \rightarrow (1, 0)$, so that the direction of the rolls turns in an anticlockwise direction as viewed from above

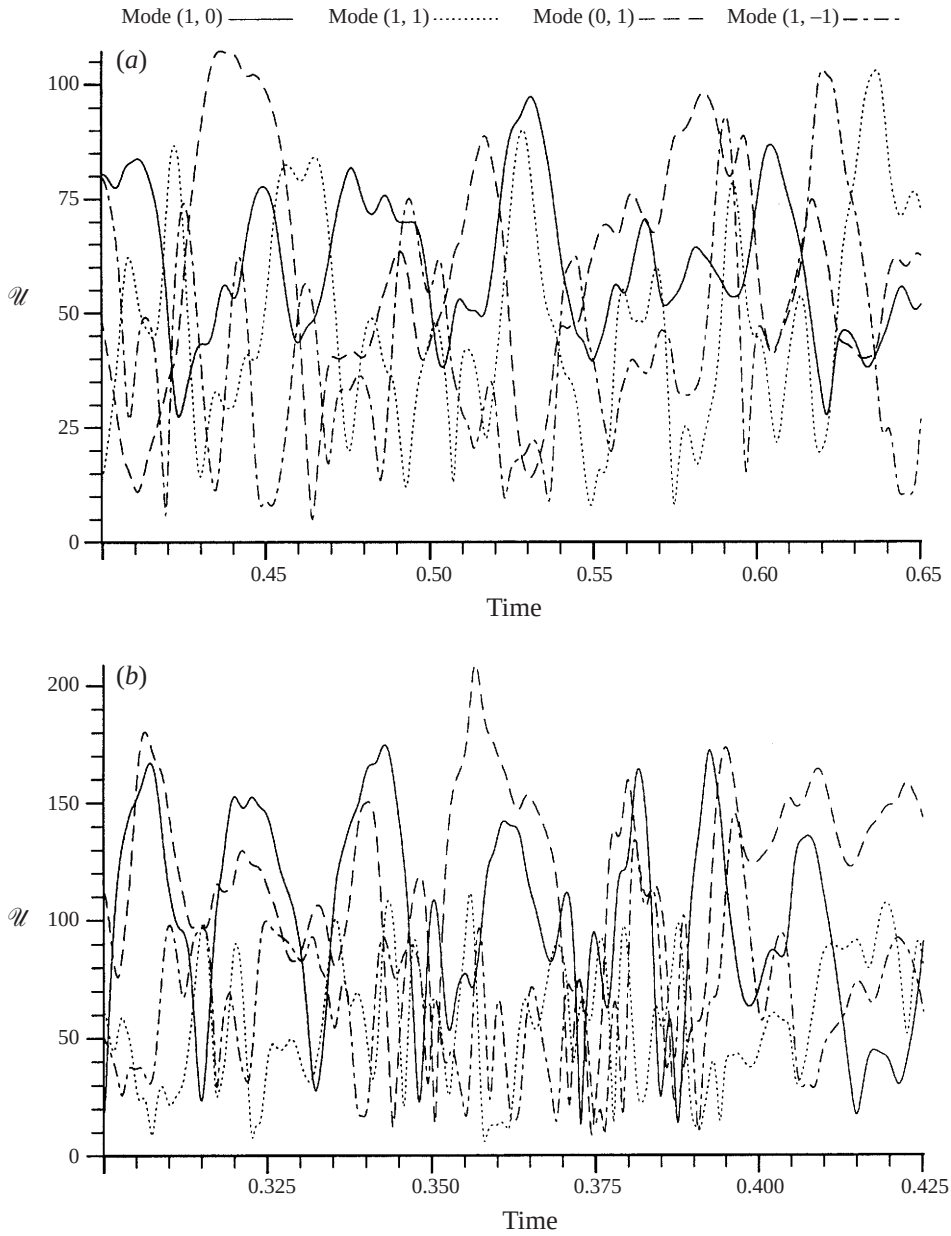

FIGURE 3. As for figure 2 but the amplitudes rather than their logarithms are shown. (*a*) $Ra = 500$, $E = 0.001$, $\alpha = \beta = 2\pi$; (*b*) $Ra = 1000$, $E = 0.001$, $\alpha = \beta = 2\sqrt{2}\pi$.

(which corresponds to eastward propagation, as found in the primary bifurcation in spherical geometry) but ever more slowly. In figure 2, the amplitudes of $\mathscr{U}_{lm}$, the root-mean-square velocity of these modes, is plotted as a function of time. After a long period of integration the trajectories spend an ever increasing time close to states with alternately the $(1, 1)$ and the $(1, -1)$ modes dominant. Eventually, rounding error

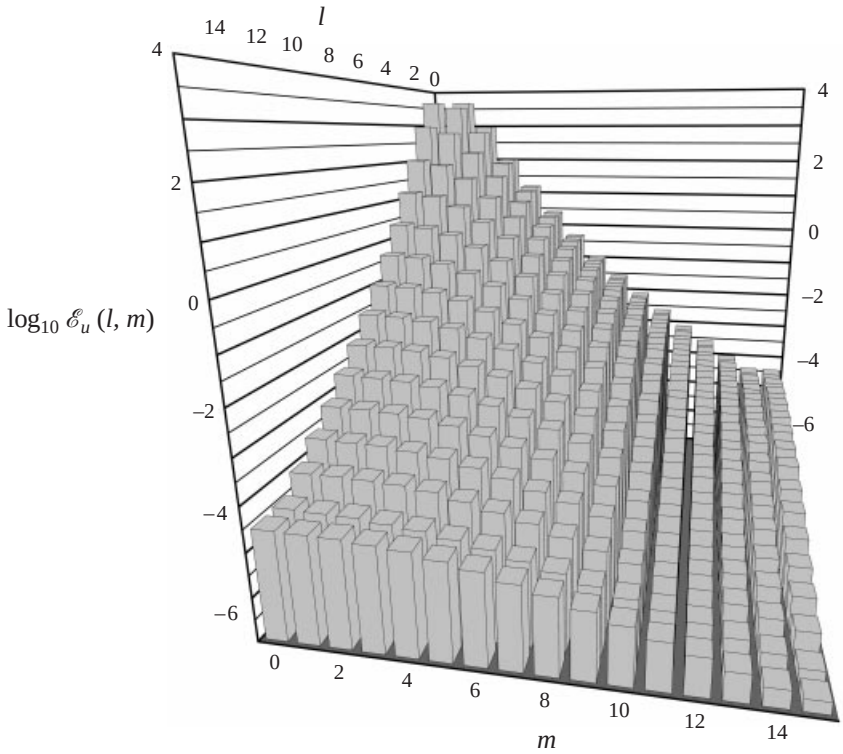

FIGURE 4. Averaged energy $\log_{10}\mathscr{E}_u(lm)$ as a function of l, m for $Ra = 1000$, $E = 0.001$, $\alpha = \beta = 2\pi$.

prevents the solution from continuing to approach the heteroclinic orbit, and some long but finite period is established. The numerical solutions shed some light on the reason for the approach to heteroclinicity. While the solution is close to the $(1,1)$ solution, the $(0,1)$ solution grows by the Küppers–Lortz instability, but the $(1,0)$ mode decays at a faster rate. In consequence, when the $(0,1)$ mode finally takes over from the $(1,1)$ mode, the $(1,0)$ mode has a very small amplitude indeed. In consequence, when the $(1,0)$ growth phase occurs, it takes even longer to bring it up to parity than during the preceding growth phase. In this way, the succeeding growth phases take longer and longer, and the rotation period tends to infinity.

If Ra is further increased the heteroclinic orbit becomes unstable. A complete analysis of the bifurcations in this region has not been performed as the behaviour is rather complex. Steady $(0,1)$ and $(1,0)$ solutions can be found in periodic windows, but by $Ra = 500$ chaotic time-dependence is found; $\mathscr{U}_{lm}$ is plotted in figure 3(a) as a function of time (over one thermal diffusion time) for each of the four modes listed above for $E = 10^{-3}$ with $\alpha = \beta = 2\pi$. Although the time-behaviour is no longer simple the modes still alternate in time, though now sustained periods of close proximity to one dominant mode do not occur. Figure 3(b) presents the equivalent picture for $Ra = 1000$, $E = 10^{-3}$ with $\alpha = \beta = 2\sqrt{2}\pi$. Note that the increase in Rayleigh number has increased the velocities and hence the magnetic Reynolds number, and has also increased the frequency of oscillation. Another difference is that in the narrower box the modes $(0,1)$ and $(1,0)$ dominate over the $(1,1)$ and $(1,-1)$ modes as might be expected.

Once the Rayleigh number is large enough for the chaotic Küppers–Lortz regime

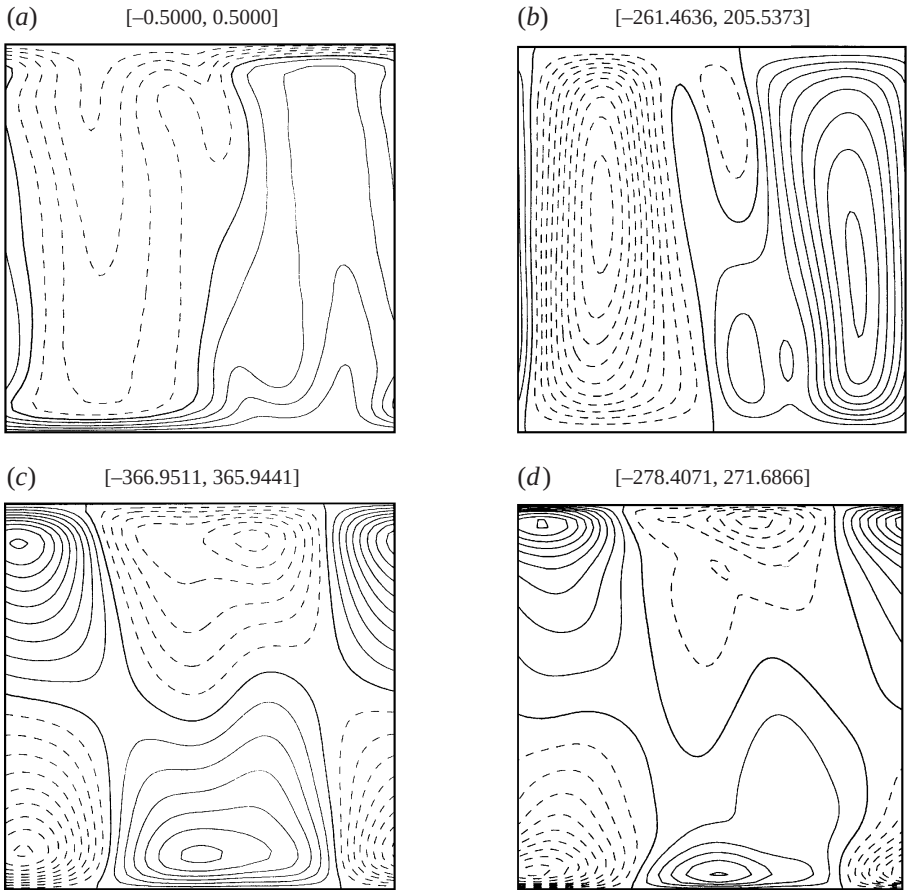

FIGURE 5. A snapshot of convection in the (y, z)-plane for the case $Ra = 500$, $E = 0.001$, $\alpha = \beta = 2\pi$. (*a*) Temperature at intervals of 0.1; (*b*) u_z at intervals of 25.0; (*c*) u_x at intervals of 40.0. (*d*) u_y at intervals of 30.0.

to become established, the nature of the convection did not change substantially with further increase of *Ra*, at least up to *Ra* about 20 times critical, which was the upper limit of *Ra* that we considered. For Rayleigh numbers of this order, reasonable solutions could be found without using very large truncations; the distribution of energy over the modes is shown in figure 4 for $Ra = 1000$, $E = 10^{-3}$, with $N_x = N_y = N_z = 16$. The procedure is to average the energy of each mode over time and then plot it on a logarithmic scale. The energy in the modes with $|l|+|m| \leqslant 16$ is about four orders of magnitude less than the energy in the low-order modes. A snapshot of the flow in the (y, z)-plane for $Ra = 500, E = 10^{-3}$ with $\alpha = \beta = 2\pi$ is shown in figure 5. Note that the vertical velocity correlates well with the temperature, as we would expect. The flow was not in a pure x-roll state at the time of the snapshot, but was approximately so, and the y-component of velocity is much as would be anticipated from continuity with the vertical flow. The x-component of velocity also has the form that is expected in rotating convection rolls: in non-rotating two-dimensional convection the fluid particles move on planes perpendicular to the roll-axis, but in rotating convection the plane containing the streamlines is rotated so it is no longer perpendicular to the roll axis (see p. 109 of Chandrasekhar 1961). In consequence,

Run	Ra	E	q	α	β	N_x	N_y	N_z
A	500	10^{-3}	5	2π	2π	32	32	24
B	500	2×10^{-4}	5	2π	2π	24	24	24
C	500	10^{-3}	1	2π	2π	16	16	16
D	500	2×10^{-4}	1	2π	2π	24	24	24
E	1500	10^{-3}	1	2π	2π	24	24	24
F	1000	10^{-3}	1	2π	2π	24	24	24
G	1000	10^{-3}	1	$2\sqrt{2}\pi$	$2\sqrt{2}\pi$	16	16	16

TABLE 2. Parameters for the runs studied.

at low E there is a strong flow parallel to the roll axis more or less in phase with the y-component of velocity, and this is quite evident in figure 5. Note also that the flow to and from the rigid boundaries gives rise to strong horizontal flows, through the Ekman layers. The Chebyshev technique resolves these layers efficiently, but nevertheless more vertical modes are required when E is decreased.

4. The plane layer dynamo

All three-dimensional dynamo simulations require substantial computer resources, even in this comparatively simple Cartesian geometry. Our freedom to explore parameter space is therefore limited and we must avoid situations where long initial transient times are needed to determine the nonlinear behaviour of the system. Situations where the convection can spend long periods in one pattern and then move into another are to be avoided if possible: there is clearly a danger of 'false' dynamo action if the pattern in which the convection is trapped for a long time is favourable for magnetic field growth, giving the impression that the system is a dynamo, even though the field decays to zero when that pattern is lost. An example of such behaviour has been given recently by Brummell, Cattaneo & Tobias (1998).

The cases which have been considered in detail are shown in table 2. The truncation parameters shown are typical; some (usually shorter) runs were performed at larger truncations, to check resolution.

4.1. *The general effect of varying the parameters*

The effect of changing q is perhaps the simplest to understand. If the magnetic field is infinitesimal or so weak as to have no significant effect on the fluid motions, the system is said to be in a 'kinematic' state. The fluid motions can be solved for first and, armed with that $\boldsymbol{u}$, we can determine $\boldsymbol{B}$ by solving (2.2), (2.4) and the appropriate boundary conditions. As we saw in § 3, the fluid velocity is independent of η and therefore of q. An increase in q merely scales up the magnetic Reynolds number, so that, at $q = 5$ for example, the convective velocity and hence R_m are simply 5 times greater, i.e. the velocities in figures 3 and 5 when multiplied by 5 give the corresponding $q = 5$ flows. Such an increase in R_m has, of course, a substantial effect on the evolution of $\boldsymbol{B}$, and the solution may quickly be driven from the kinematic regime and into a magnetohydrodynamic state where the back reaction of the field on the flow cannot be ignored. Computationally, the disadvantage of increasing q is that finer scale magnetic structures occur, requiring increased resolution. We note here that we shall later broaden the use of the term 'kinematic' by also using it to

describe solutions where the magnetic field, though not infinitesimal, is insufficiently strong enough to alter the magnitude or character of the flow significantly.

Increasing Ra increases the convective velocity, and hence also raises R_m. Thus at fixed q one would expect dynamo action to occur provided Ra is large enough. The effect of varying E is less easily predicted. As E is reduced, the dominant horizontal wavelengths shorten, and the critical Rayleigh number increases. However, in the range of numerically accessible E the rise in Ra_c is not great, and the flow is strongly convectively supercritical when the chaotic Küppers–Lortz regime is reached. We expect rotation to enhance the helicity, so we may expect lower values of E to favour dynamo action, and this is consistent with our results.

4.2. *Onset of dynamo action*

Since it was anticipated that small E would favour dynamo action, our first numerical run ('Run A') assumed $E = 0.001$ and with $R = 500$ and $q = 5$. The wavenumbers chosen were $\alpha = \beta = 2\pi$; the truncation parameters were set at $N_x = N_y = 32, N_z = 24$ though, in the magnetically saturated regime, a smaller truncation is adequate for reasons discussed below. Because the system is chaotic, runs with different truncations diverge quite quickly even when started from the same initial conditions. The starting procedure adopted was first to run the convection-only code (the code with the magnetic field switched off, starting with a small random seed temperature disturbance). Since the Rayleigh number is well above the critical value for convection, the disturbance grows rapidly. After the transients in the convection-only flow had disappeared, a small random magnetic field seed field was switched on. Care had to be taken to ensure all possible wavenumbers were present in the seed fields; in one example run, a seed field containing only modes of even $l + m$ was imposed. Modes of odd $l + m$ were then not induced by the nonlinear interactions, and remained zero throughout the calculation. The behaviour of the resulting solution was then quite different from typical solutions when odd $l + m$ modes are also present.

The logarithm of the magnetic energy in the toroidal, poloidal and mean components of the field are shown in figure 6(*a*), where it is clear that all components of the field grow until a saturated state is reached. Two phases are evident: a regime of kinematic growth where the Lorentz force is comparatively negligible followed by a magnetically saturated regime where the Lorentz force controls the magnetic field amplitude.

The second run shown in figure 6(*b*) (Run G) is for $\alpha = \beta = 2\sqrt{2}\pi$, $q = 1$, $Ra = 1000$. At these values of q and Ra the cubical box solution was not a kinematic dynamo; the seed magnetic field decayed slowly. By narrowing the box by a factor of $\sqrt{2}$ in both directions a rather strong kinematic growth was obtained. A further advantage of this solution is that, as growth is obtained at comparatively low magnetic Reynolds number, a truncation of $N_x = N_y = N_z = 16$ is adequate. (A run with a truncation of $N_x = N_y = N_z = 24$ grew at the same rate and to the same saturation level.)

Interestingly, although the cubical box $\alpha = \beta = 2\pi$ does not give a kinematic dynamo at $Ra = 1000$, $q = 1$, $E = 10^{-3}$, a completely stable nonlinear dynamo can be obtained at these parameters by starting with a fully developed magnetic field taken from a solution at different parameter values (the Run A values were generally used). Indeed, a stable nonlinear dynamo was obtained at $Ra = 500$, $q = 1$, $E = 10^{-3}$ in the cubical box, as shown in figure 6(*c*). Thus the problem of magnetic field generation is quite subcritical; the magnetic field acts on the flow in a way that aids the field generation process. It should however be noted that this effect may

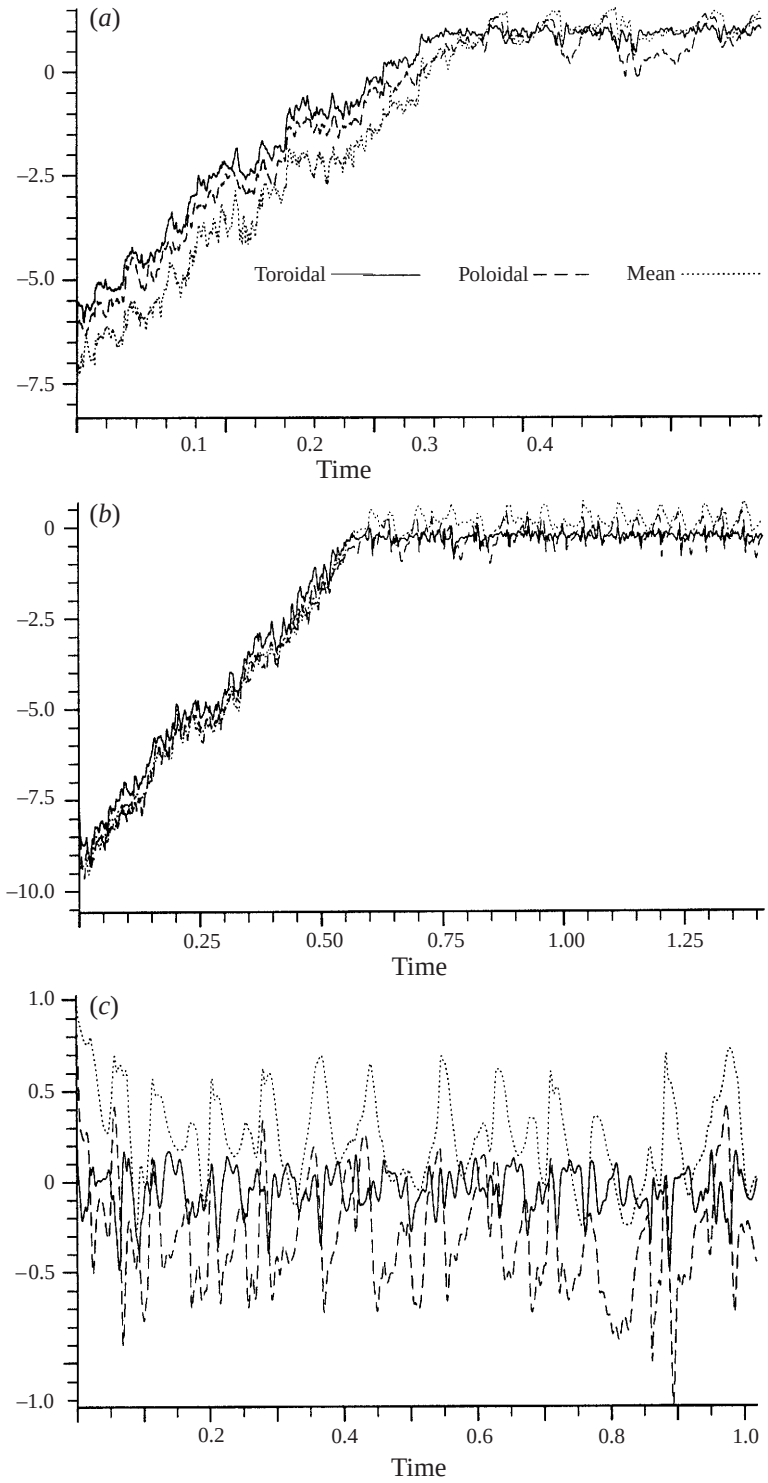

FIGURE 6. Magnetic energy as a function of time for (*a*) Run A ($Ra = 500$, $q = 5$, $E = 0.001$, $\alpha = \beta = 2\pi$). (*b*) Run G ($Ra = 1000$, $q = 1$, $E = 0.001$, $\alpha = \beta = 2\sqrt{2}\pi$). (*c*) Run C ($Ra = 500$, $q = 1$, $E = 0.001$, $\alpha = \beta = 2\pi$); this case is subcritical only. The toroidal, poloidal and mean field energies, $\log_{10}\mathscr{T}$, $\log_{10}\mathscr{P}$ and $\log_{10}\mathscr{M}$, respectively, are plotted.

well depend on the size of the periodic box. A possible reason why the narrower boxes are preferred for field generation is that for these boxes the roll solutions $(1,0)$ and $(0,1)$ are more favoured, and the convection pattern, although chaotic, spends much more time alternating between these modes. This form of convection appears to favour dynamo action. In the cubical periodic box, all four modes $(1,0)$, $(1,1)$, $(0,1)$, and $(1,-1)$ alternate rather randomly (see figure 3) which seems less favourable for dynamo action. When the magnetic field is present, there is a tendency for the modes of the longer wavelength, namely the $(1,0)$ and $(0,1)$ rolls, to dominate even in the cubical box, thus producing the convection pattern most favourable for dynamo action.

4.3. *Kinematic regime*

Although the field energy fluctuates during the growth phase, there is a fairly well-defined growth rate in this phase. Both Runs A and G showed similar behaviour during the growth phase. The flow in the kinematic regime is of course much the same as in non-magnetic chaotic convection.

The morphology of the magnetic field is rather different during the kinematic phase from that in the saturated regime analysed below. The growing field consists of 'cigar-like' structures in which high wavenumbers dominate. A snapshot of the field during the kinematic growth phase is shown in figure 7. The nature of the cigar-like structures is best seen in an isosurface plot on which the surface at which $|\boldsymbol{B}|$ attains 40% of its maximum value; see figure 7(*e*). The volume enclosed by this surface is a remarkably small percentage of the total volume of the periodic box, showing the concentrated nature of the generated fields. Similar behaviour has been found in fast dynamo simulations (Childress & Gilbert 1995). A snapshot of the two-dimensional energy spectrum (over modes (l,m)) in the kinematic regime is displayed in figure 8. Figure 8(*a*) shows $\log_{10}\mathscr{E}_u(l,m)$, the power spectrum of $\boldsymbol{u}$ and figure 8(*b*) shows $\log_{10}\mathscr{E}_m(l,m)$, the power spectrum of $\boldsymbol{B}$; these snapshots were taken from the kinematic part of Run A. Note that the power spectrum of $\boldsymbol{u}$ falls off much more rapidly than the power spectrum $\boldsymbol{B}$, reflecting the small-scale field structures generated by the kinematic dynamo.

The growth of the magnetic field is somewhat erratic on short timescales, with phases of little or no growth followed by spurts of strong activity. This reflects the fact that the convection is time-dependent, with a fluctuating convection pattern; for some patterns strong field growth occurs, others merely enhance magnetic dissipation. Nevertheless, averaged over the whole kinematic phase, the growth is evidently exponential with a reasonably well-defined growth rate.

4.4. *Saturated regime*

In both the runs where kinematic dynamo action has been established, there is a fairly well-defined time at which the field ceases to grow, and a magnetically saturated regime, with a statistically steady field strength, is reached. In the subcritical cases (Runs C, E and F) the form of the saturated state was broadly similar to the Runs A and G which are kinematic dynamos. The Küppers–Lortz mechanism still operates, with the convection having the form of an approximately two-dimensional roll which rotates irregularly, and the mean component of the magnetic field also rotates in such a way as to be approximately lined up with the roll axis; Soward (1974) noted that a single roll with rotating orientation can act as a dynamo. A similar scenario, but without the effect of rotation, has been noted by Gog *et al.* (1999).

A snapshot of the saturated field and flow taken from Run C is shown in figure 9.

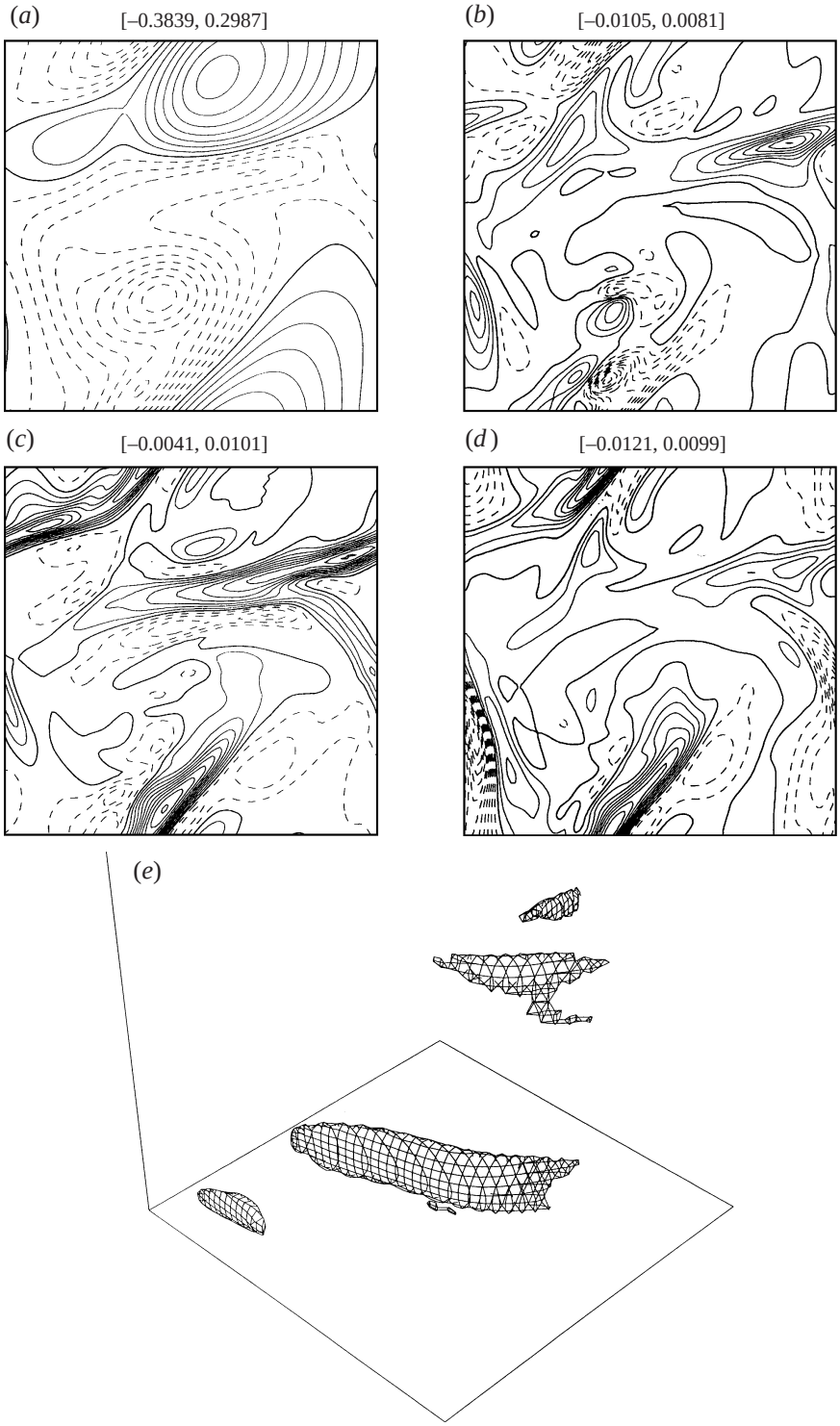

FIGURE 7. A snapshot of magnetic field in the (x, y)-plane $z = 0.3$ for the case $Ra = 500$, $E = 0.001$, $q = 5$, $\alpha = \beta = 2\pi$ (Run A) in the kinematic regime. (*a*) Temperature at intervals of 0.04; (*b*) B_z at intervals of 0.001; (*c*) B_x at intervals of 0.001; (*d*) B_y at intervals of 0.001; (*e*) Isosurface of the magnetic field strength at 40% of the peak field.

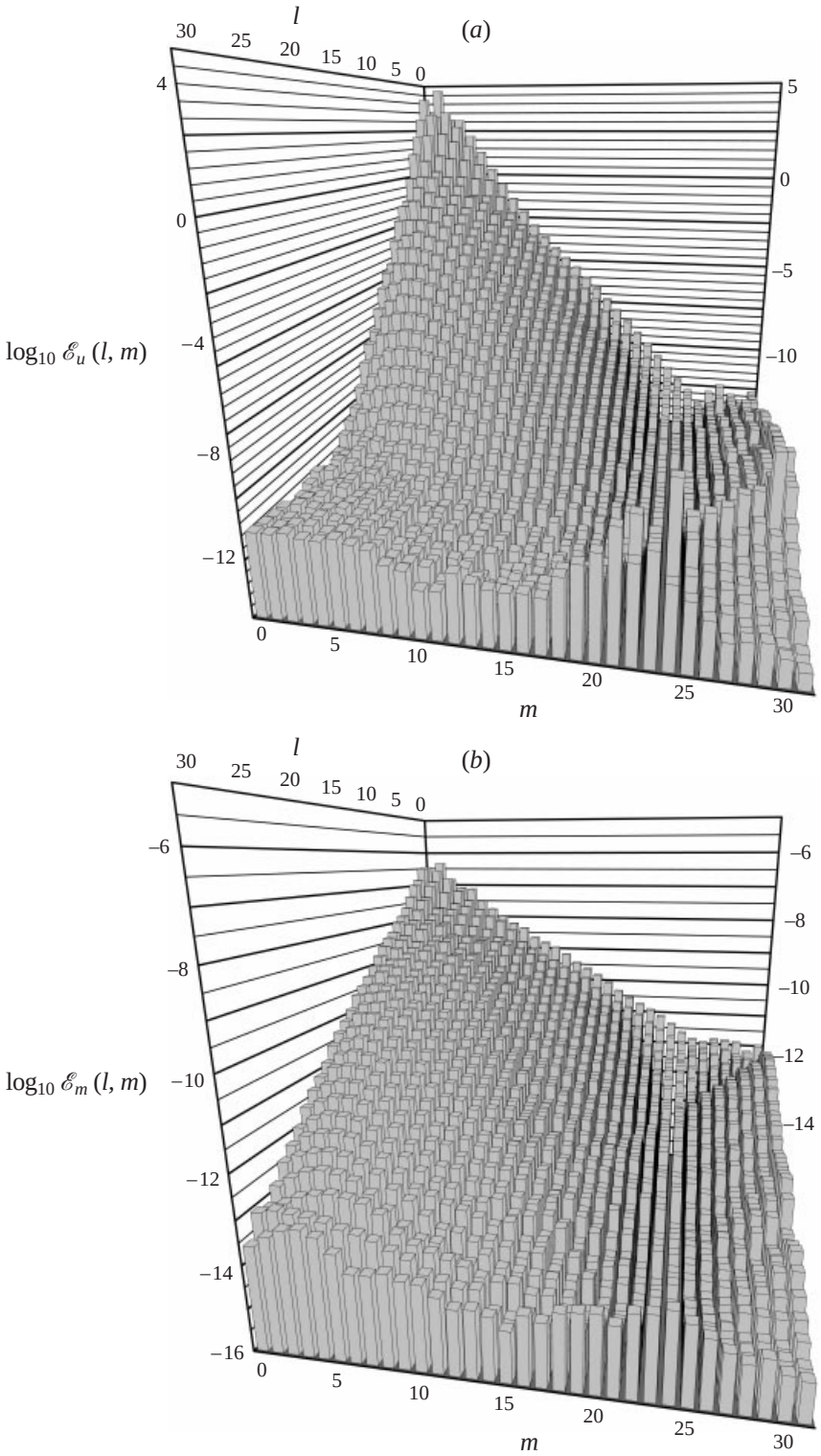

FIGURE 8. Spectral coefficients as a function of l, m for Run A in the kinematic regime. (*a*) Kinetic energy $\log_{10} \mathscr{E}_u(lm)$. (*b*) Magnetic energy $\log_{10} \mathscr{E}_m(lm)$.

The temperature contours in the (x, y)-plane displayed in figure 9(a) reveal that the convection at this time is approximately an x-roll in which the $(0, 1)$ component is dominant. The vertical field plot (figure 9(b)) confirms this. The view in the (y, z)-plane, perpendicular to the roll, shows a hot rising plume and a cold descending plume (compare figures 9c and 9h). Note that the negative B_y field in figure 9(f) has been stretched out into vertical field by the plumes; see figure 9(d). (The magnitude of the positive B_y field at the centre of the cell is much weaker than the negative B_y field nearer the boundaries.) This vertical field has opposite signs on either side of the plume as expected; this effect can also be seen in figure 9(b). The flow along the roll is seen in figure 9(g) (which may be compared with figure 5) and this flow stretches out x-field which is predominantly positive in the central regions and negative near the boundaries. In the next section we put these observations together to form a model of the dynamo generation process.

Note that the final state has no symmetry about the mid-plane, as we would expect given that there is no particular symmetry in the horizontal pattern. Modes with u_z symmetric about $z = 0$ and u_x and u_y antisymmetric are preferred at onset, and even in the the strongly nonlinear regime the flow shows a tendency to adopt this symmetry approximately.

The time-dependence in the saturated state is illustrated in figures 10(a) and 10(b), which are for Run C parameter values. In figure 10(a) the velocity amplitudes of the four modes are plotted as a function of time. If we compare that with figure 3(a), which is for non-magnetic convection only with the same box size and Ra and E, we see that the magnetic field has enhanced the importance of the $(0, 1)$ and $(1, 0)$ modes at the expense of the $(1, 1)$ and $(1, -1)$ modes. Thus the magnetic field has had a similar effect to reducing the box size, and both effects assist magnetic field generation. Also, the magnetic field has restored the sequence in which the modes appear, and which is so evident in figure 2. In figure 3(a), at $Ra = 500$ but with no magnetic field, the time ordering of the modes looks rather random. Thus the magnetic field seems to have partially restabilized the rotation of the convection rolls which occurred at lower Ra following the Küppers–Lortz instability. In figure 10(b), the amplitude of the total magnetic energy $\mathscr{E}_m$, the z-averaged amplitude of the mean field $(\bar{b}_x^2 + \bar{b}_y^2)^{1/2}$, and the field phase angle (the mean field direction $\tan^{-1} \bar{b}_y/\bar{b}_x$) are plotted against time. We can compare figures 10(a) and 10(b) to see how the field correlates with the changing convection pattern. The mean field direction correlates strongly with the roll axis; the field turns through 2π as the convection goes through a full cycle. At $t = 0.06$, the $(0, 1)$ mode, a roll with axis in the x-direction, is dominant and the mean field makes a zero angle with the x-axis. At $t = 0.12$, the $(1, 0)$ roll is dominant, and the field angle is now $\frac{1}{2}\pi$. The field is somewhat suppressed at $t = 0.19$ when the $(1, 1)$ mode is dominant, but recovers at $t = 0.24$ to make an angle of π with the x-axis and so on. The period of the cycle is approximately 0.35 dimensionless units.

The rotation of the convection pattern is achieved by the four modes discussed in § 3 successively growing and decaying. In consequence, the flow is more three-dimensional during the transition from one mode to the next than it is when one of the modes completely dominates the rest. It is noticeable that the total field energy grows most when the flow is most three-dimensional, and decays when the flow is most two-dimensional, i.e. when one of the rolls dominates the others. (Note that the maximum field is in phase with the time of maximum dominance of a particular mode.) In consequence, the field strength oscillates during the cycle, growing at the transition times and decaying when the flow is too two-dimensional.

During the kinematic regime, the energy in the mean field is significantly smaller

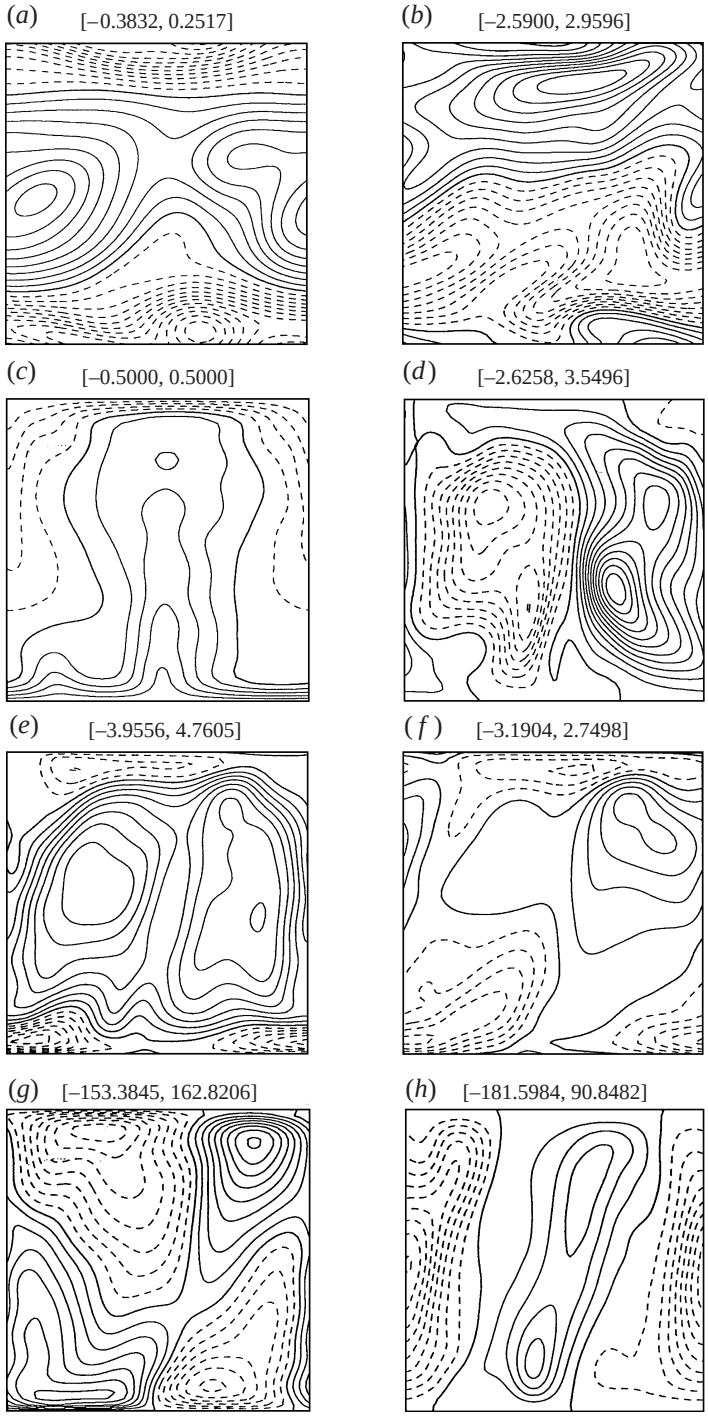

FIGURE 9. A snapshot of magnetic field for the case $Ra = 500$, $E = 0.001$, $q = 1$, $\alpha = \beta = 2\pi$ (Run C), the subcritical case in the saturated regime. (*a*) Temperature at intervals of 0.03 in the (x, y)-plane $z = 0.25$. (*b*) B_z at intervals of 0.3 in the (x, y)-plane $z = 0.25$. (*c*) Temperature at intervals of 0.1 in the (y, z)-plane. (*d*) B_z at intervals of 0.3 in the (y, z)-plane. (*e*) B_x at intervals of 0.6 in the (y, z)-plane. (*f*) B_y at intervals of 0.6 in the (y, z)-plane. (*g*) u_x at intervals of 20.0 in the (y, z)-plane. (*h*) u_z at intervals of 20.0 in the (y, z)-plane.

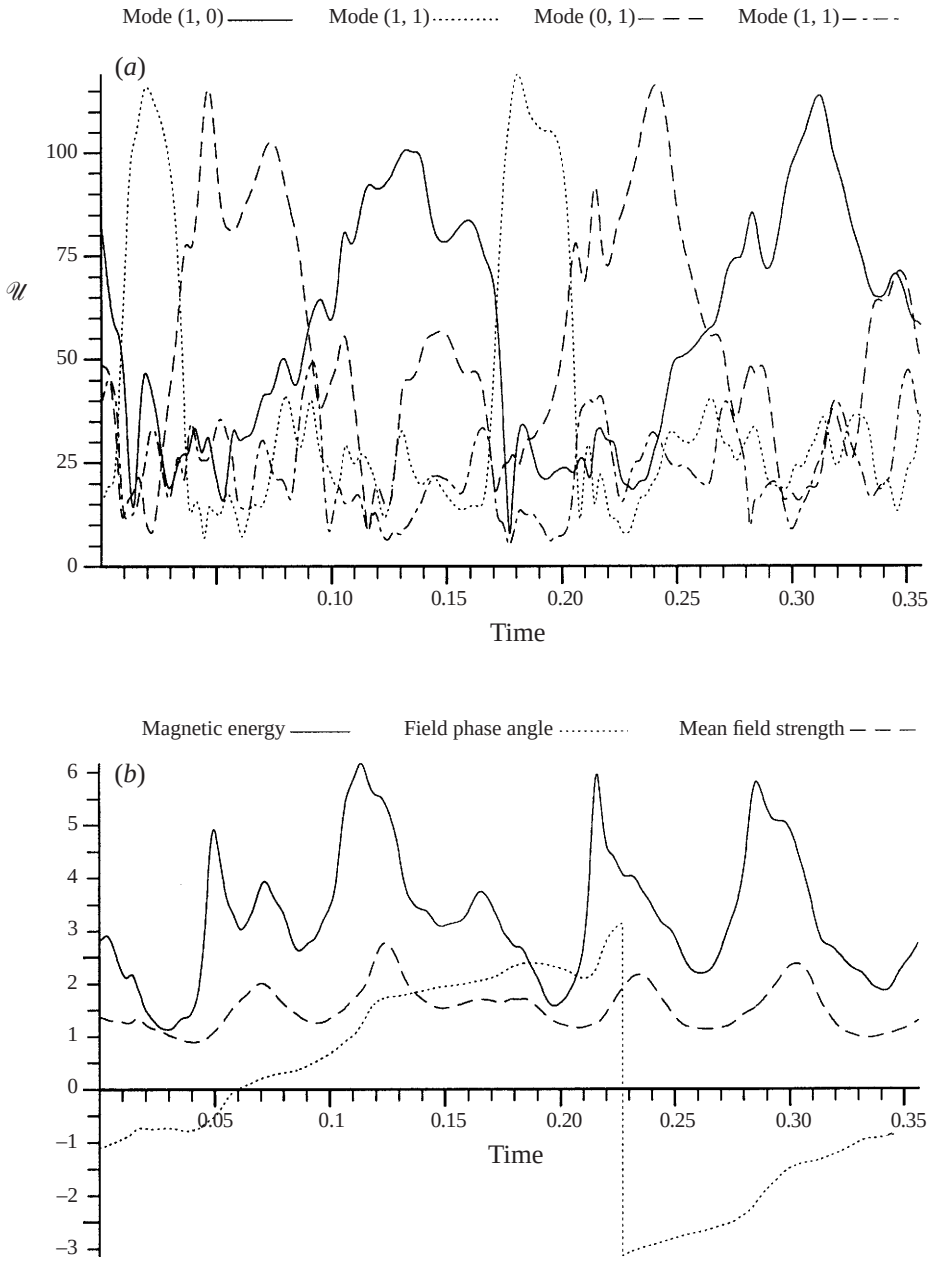

FIGURE 10. (*a*) The root-mean-square velocity, $\mathscr{U}_{lm}$, of the modes $(1,0)$, $(1,1)$, $(0,1)$ and $(1,-1)$, as a function of time in the saturated cycle for $Ra = 500$, $E = 0.001$, $q = 1$, $\alpha = \beta = 2\pi$. (*b*) Total magnetic energy $\mathscr{E}_m$, the mean field $(\bar{b}_x^2 + \bar{b}_y^2)^{1/2}$ and the mean field phase angle $\tan^{-1} \bar{b}_y/\bar{b}_x$ as functions of time.

than the energy in toroidal and poloidal components. This is however reversed in the saturated field, where the mean field is as large or larger than the horizontally fluctuating components (figures 6(*a*) and 6(*b*)). This is part of a more general trend in which the magnetic energy moves down the spectrum as saturation occurs, the so-called 'inverse cascade' (Gilbert & Sulem 1990). It can be seen crudely by comparing

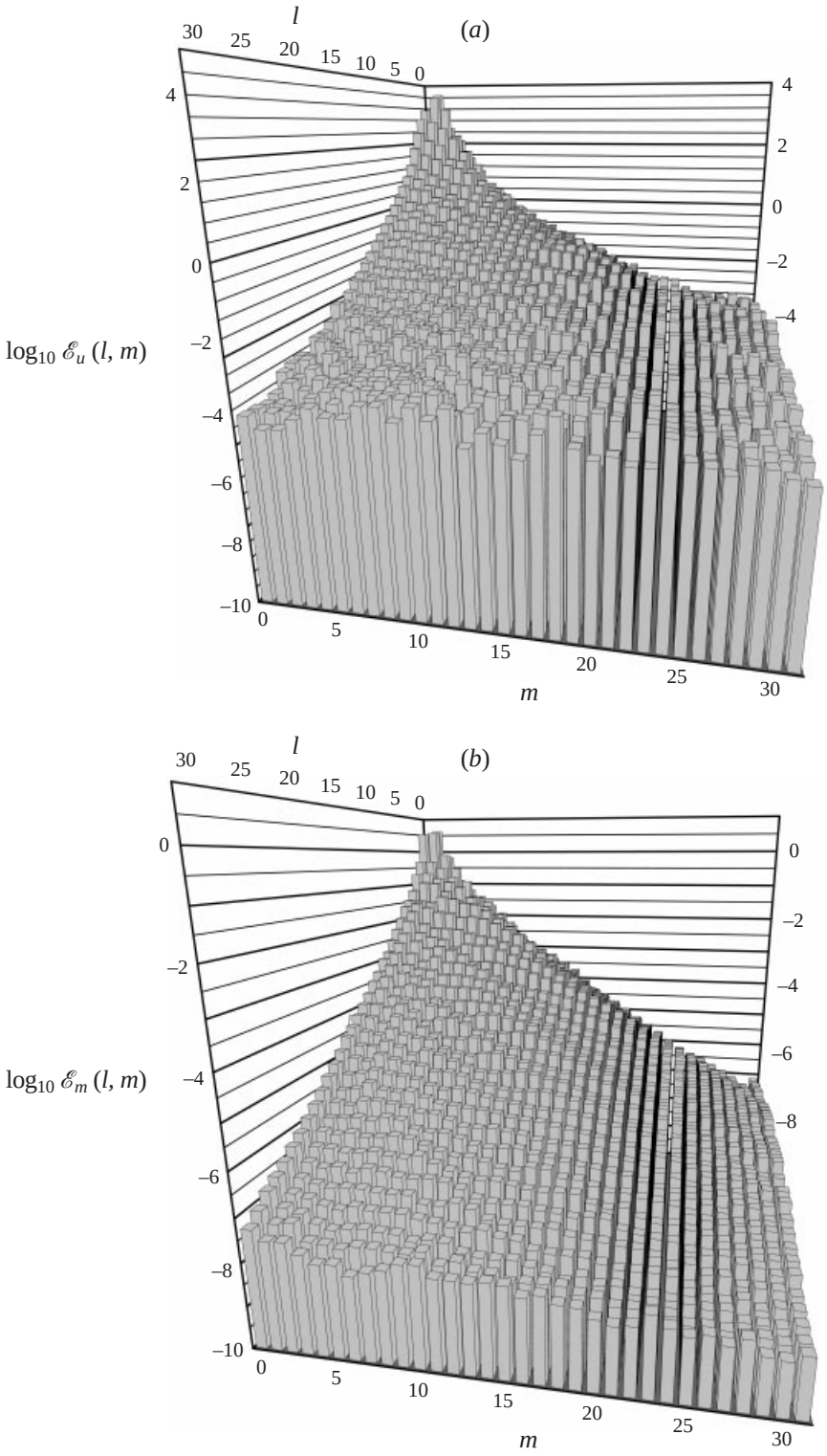

FIGURE 11. Spectral coefficients as a function of l, m for Run A in the saturated regime. (*a*) Kinetic energy $\log_{10} \mathscr{E}_u(lm)$. (*b*) Magnetic energy $\log_{10} \mathscr{E}_m(lm)$.

the snapshots of the field in the saturated state (figure 9) with the kinematic snapshot (figure 7). A more systematic view can be obtained by comparing the energy spectrum (over modes (l,m)) in the saturated regime, shown in figure 11, with the corresponding figure 8 for the kinematic regime. Figure 11(a) presents $\log_{10}\mathscr{E}_u(l,m)$, the power spectrum of $\boldsymbol{u}$ and figure 11(b) displays $\log_{10}\mathscr{E}_m(l,m)$, the power spectrum of $\boldsymbol{B}$ taken from a snapshot in the saturated part of Run A. Note that in the kinematic regime the magnetic energy ranges over only 6–7 orders of magnitude from $(1,0)$ to $(1,31)$, while kinetic energy ranges over about 16 orders of magnitude for the same range of wavelengths. In the saturated regime, the magnetic energy range is greater, so that the energy has become more concentrated in the longer wavelengths while the kinetic energy range is much shorter, with the result that there is much more power in shorter wavelengths than for the kinematic regime. This has implications for the numerical method: to study pure convection (at moderate Ra and E) it is possible to use relatively low truncations, whereas for the kinematic dynamo regime we need rather high truncations for the field. As we approach the saturated regime, the need for the high resolution for $\boldsymbol{B}$ is reduced, although greater resolution is required for $\boldsymbol{u}$. In practice, saturated solutions are, overall, easier to obtain than kinematic solutions as the savings on $\boldsymbol{B}$ outweigh the extra work required on $\boldsymbol{u}$.

An important issue is to discover the mechanism by which saturation takes place. It is sometimes assumed that saturation occurs at approximate equipartition of kinetic and magnetic energy, on the grounds that the inertial stresses then approximately balance the magnetic stresses in the momentum equation. This is clearly inappropriate in our case, as inertial terms are ignored in this calculation. Here a balance between Lorentz and Coriolis forces is more appropriate, so we expect saturation to occur at Elsasser number of order unity. In the geodynamo, which motivated our study, the inertial forces are also small, and balancing Lorentz and Coriolis forces gives a sensible estimate for the field strength in the core. The magnetic energy in the Earth's core is many orders of magnitude greater than its kinetic energy (as measured in the rotating frame).

Figures 6(a) and 6(b) indicate that the field saturates at an Elsasser number slightly greater than unity, showing that the Lorentz force is playing a significant role in the saturation process, as expected. The average velocity is slightly lower in the saturated regime than in the kinematic regime, in line with the naïve view that the Lorentz force impedes the flow, as expected from magnetoconvection theory. In Run G, the kinetic energy averaged over the kinematic regime was approximately 10 100 and the equivalent value averaged over the saturated regime was 7250, corresponding to averaged magnetic Reynolds numbers of 142 and 120 respectively. The corresponding typical average magnetic Reynolds numbers in Run A are about 630 in the kinematic regime and 450 in the saturated regime. We cannot, however, simply explain the saturation as a reduction of the flow velocity to the critical value at which dynamo action occurs; the form of the convection is very important. When Ra is smaller, R_m in the saturated regime is smaller than the saturated R_m at larger Ra.

5. A model of the dynamo

In addition to the snapshots of the field and the flow, we have also studied videos of the solutions. On the basis of these we present a simplified picture of the dynamo process. The observed fields and flows are chaotic, with a significant amount of small-scale structure, so it is not easy to identify the essential processes from the inessential 'detail'. The picture described below was obtained by emphasizing the role of the

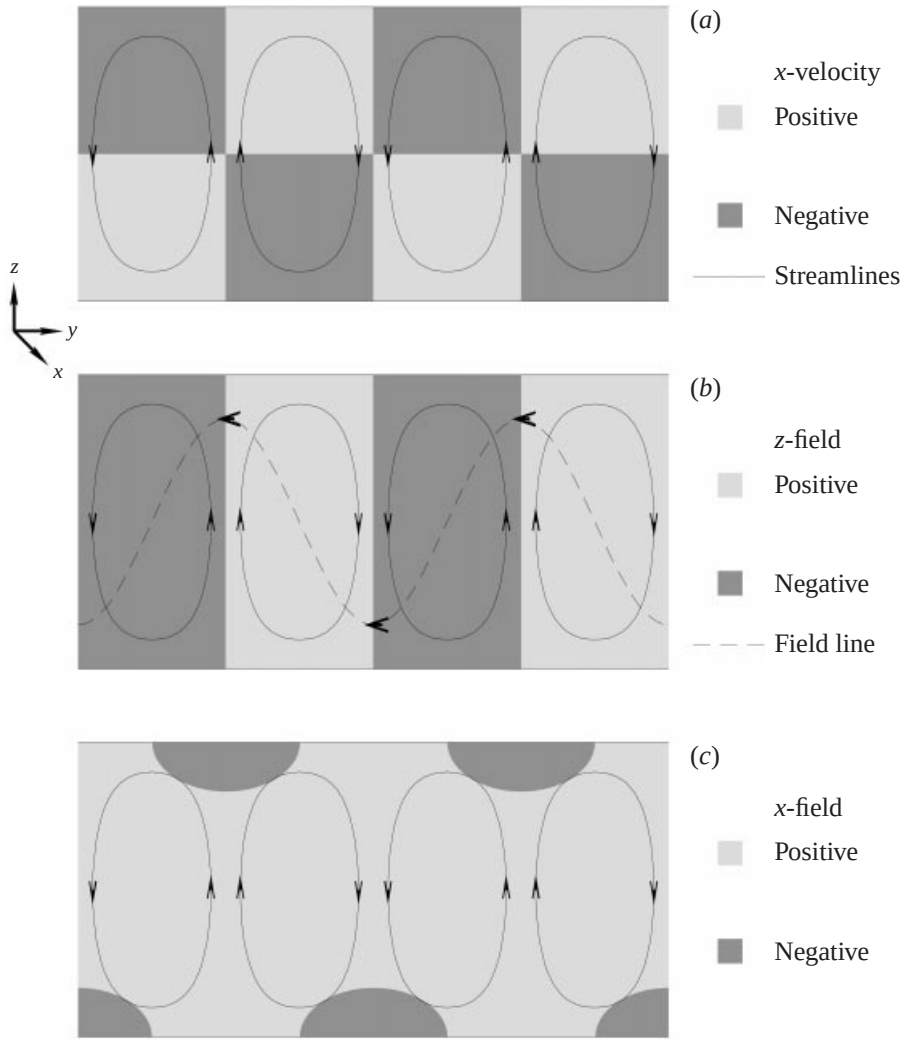

FIGURE 12. (a, b, c) Cartoon of the model for dynamo action.

terms in the induction equation that seem to be dominant, and ignoring the rest. The picture does seem to fit the behaviour observed in the runs performed, and it can be compared with the snapshot of the true solution shown in figure 9. It is hoped the model may prove useful in developing physical understanding of the essence of the dynamo mechanism, and hence in developing an intuition for dynamo action in different parameter ranges.

We start with the convection modelled by two perpendicular rolls which alternate approximately sinusoidally in time. We can identify these with the $(1, 0)$ and $(0, 1)$ rolls. Suppose at time $t = 0$ the x-roll $(0, 1)$ is dominant. Because the convection roll is in a rapidly rotating environment, there will be strong flows along the x-roll as indicated in figures 5(c) and 9(g) and idealized in the cartoon shown in figure 12(a); see also Chandrasekhar (1961). The vertical motion is closely aligned with hot rising fluid and cold falling fluid, as expected, and the alignment of the horizontal flow along the roll is a very robust feature of nonlinear convection.

The mean field will be primarily aligned in the x-direction, but since the y-roll has only recently decayed, a component of the field in the y-direction remains, and we assume that initially this y-component of field is approximately uniform across the layer and negative. The velocity field of the x-roll will act on this y-field to stretch out new vertical fields as indicated in figure 12(b). Note that the vertical fields are out of phase in y with the rising and falling plumes, occurring principally in the roll centres.

Now consider the x-component of the field stretched out by the rotation-induced flows in the x-direction. In the middle of the layer the vertical velocity shear is dominant, and this stretches out positive x-field (see figure 12(c)). Note that, because the induced vertical field is in phase in y with the x-velocity, positive x-field is generated in every cell centre. However, negative x-field is induced near the boundaries by the horizontal shear acting on the original horizontal y-field, indicated by the dark semi-elliptical regions in figure 12(c). Indeed, if we consider a single field line, since it has no x-component of velocity at the y-coordinates of the rising and falling plumes, there must be just as much stretching in the negative x-direction as in the positive x-direction. The important point is that the negative x-field, because it is created near the insulating boundary, escapes from the system quite quickly. Recall that, according to the argument below (2.23), no net field $\bar{b}_x$ or $\bar{b}_y$ can develop if the boundaries are perfectly conducting, so that any mechanism that generates mean field in our model must invoke diffusion of field out of the boundaries at some stage. In consequence, we are left with a net positive mean field in the x-direction.

If the roll remained two-dimensional, our mechanism could not sustain a dynamo since we originally assumed an approximately uniform y-directed field which is not regenerated. With the gradual diffusion away of the y-component of the field, the larger mean field in the x-direction will also start to fall. At this point, however, the roll turns through 90°, so that the mean positive x-field is now perpendicular to the roll. With the roll turned through 90°, this old mean field is exactly what is needed to start the next quarter of the cycle off again. The mean field produced in this second quarter of the cycle is in the positive y-direction. After a further 90° turn, this positive y-field serves as the seed for the roll which is now aligned again in the x-direction generating negative x-directed field in the third quarter of the cycle, and in the last quarter of the cycle the negative y-directed field which was required at the start of the cycle is generated.

This picture fits in with the results shown in figures 10(a) and 10(b). The start of the cycle given above occurs at about $t = 0.03$ where the x-roll is established and building. The mean field (the dashed line) is starting to build in the x-direction (phase angle 0), using the previous negative y-component. At $t = 0.07$ the field has peaked, and the phase angle is close to 0, i.e. aligned with the x-roll. Now there is no more y-field left to generate mean x-field, and the mean x-field starts to fall. By $t = 0.1$ the x-roll is rapidly declining and the $(1,0)$ y-roll is growing. The phase angle of the mean field rotates to $\frac{1}{2}\pi$ as positive y-field starts to build up during the second quarter of the cycle. The third and fourth part of the cycle behave similarly, except that at about $t = 0.19$ the $(1,1)$ roll makes a brief appearance. This does not seem to be effective in field generation (we ignored this mode in our model for simplicity) and the next growth of mean field starts at about $t = 0.22$ when the $(0,1)$ x-roll is strong. Again there is a sharp rise in mean field, this time in the negative x-direction (phase angle π). At this point the negative y-roll comes in and we start the fourth quarter of the cycle.

We therefore expect four peaks in the energy per cycle, defining the cycle as the

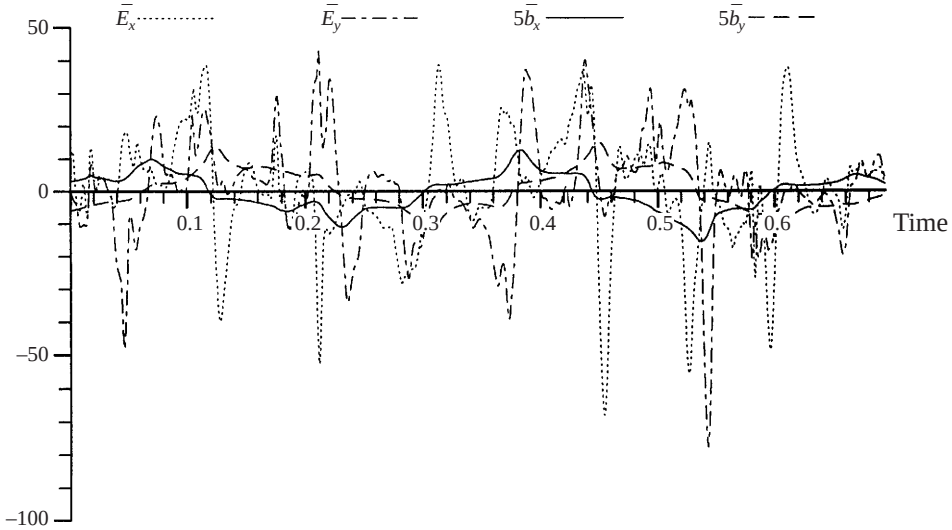

FIGURE 13. The weighted horizontal components of the e.m.f. $\bar{E}_x$ and $\bar{E}_y$ are plotted as functions of time. Also shown are the z-averaged components of the mean field $\bar{b}_x$ and $\bar{b}_y$ scaled up by a factor 5. Parameter values are as in figure 10: $Ra = 500$, $E = 0.001$, $q = 1$, $\alpha = \beta = 2\pi$.

approximate time taken for the mean field to go through a complete rotation. The mean field is the largest contributer to the total field energy, but it is clear from figure 10(b) that the total energy peaks a little earlier than the mean field in the cycle. This can be explained by the vertical fields generated in our model mechanism which develop before they are stretched out to form the horizontal mean field.

Since α-effect models have been used extensively in the study of nonlinear dynamos, it is of interest to study the mean e.m.f. produced in our model. The horizontal components are defined as

$$E_{x,y}(z) = \langle \boldsymbol{u} \times \boldsymbol{B} \rangle_{x,y}. \tag{5.1}$$

The mean field components, b_x and b_y, have the symmetric part about $z = 0$ generally dominant over the antisymmetric part, so it is natural to take the z average as a measure of their strength. The mean e.m.f. is, however, predominantly antisymmetric about $z = 0$, so we measure its strength by including a factor z in the integral,

$$\bar{E}_{x,y} = \int_{-1/2}^{1/2} z \langle \boldsymbol{u} \times \boldsymbol{B} \rangle_{x,y} \, \mathrm{d}z, \tag{5.2}$$

so that the antisymmetric part is measured. In figure 13 we have plotted $\bar{E}_x$ and $\bar{E}_y$ along with the vertically averaged mean fields $\bar{b}_x$ and $\bar{b}_y$ as functions of time, for the same starting values as in figures 10(a) and 10(b) (though it has been run for longer). In an α-effect model, the turbulence is assumed to be on a smaller scale than the mean field, and so there is a time-independent relation between the mean e.m.f. and the mean field given by $E_i = \alpha_{ij} b_j$, with α_{ij} some constant tensor: in nonlinear models, α is sometimes allowed to vary with the mean field $\boldsymbol{b}$. The difficulty with modelling our system in this way is that the time correlation between the mean field and the mean e.m.f. is not that strong, as can be seen from figure 13. Although there is a tendency for $\bar{E}_{x,y}$ to have the same sign as $\bar{b}_{x,y}$, there are intervals of time during which they

have opposite sign, and also intervals when the components of $\bar{\boldsymbol{b}}$ are increasing while the components of $\bar{\boldsymbol{E}}$ are decreasing.

6. Low Ekman number regime

At low E the timestep has to be shortened and the resolution increased to resolve the Ekman layers, and cope with the appearance of smaller scale structures. In consequence, it is very expensive to do long runs at low E; so runs B and D were started with a finite-amplitude magnetic field. We therefore do not know whether the dynamos at these values of E can grow from small amplitude or whether they are subcritical, as runs C, E and F were. However, figures 6(a) and 6(b) suggest that, once the regime has saturated, a relatively steady state is achieved quite quickly. So although Runs B and D were continued for less than a magnetic diffusion time we feel the results are significant. Figure 14(a) gives the Run B results, and figure 14(b) the Run D results. Comparing with figure 6(a–c), we see that the most noticeable feature is that the magnetic field is stronger and the ratio of the mean magnetic field to the other (poloidal and toroidal) components is significantly greater. The larger field strength at lower E is slightly surprising, because the field strength is determined by balancing the Lorentz force in the equation of motion with the other forces, and one of those is the viscous force which is proportional to E. Indeed, for the geostrophic part of the flow the Lorentz force can only be balanced against the viscous force, and in the Ekman regime of nonlinear dynamos, $|\boldsymbol{B}|$ scales with $E^{1/4}$. This suggests that a Taylor state must have been achieved; we examine this in more detail below.

Snapshots of the field and flow for Run D are given in figure 15(a–h), which may be compared with figure 9. At lower E, smaller scales in the flow are more evident, as would be expected given that viscosity is less important. This is also reflected in smaller lengthscales emerging in the field, although the mean field is large. The larger field strengths also mean that the effect of the Lorentz force on the flow is more evident; this is best seen in videos of the flow, where the deflection of rising and falling thermal plumes by regions of strong magnetic field can be seen. Nevertheless, corroboration is provided by figures 15(c) and 15(f), where the rising thermal is seen to be blocked from reaching the top boundary by a region of strong y-field near that boundary; figure 5 shows how close the thermal plume gets to the boundaries in the absence of magnetic field. There is also a tendency, again more visible in videos, for the mean field to be weaker in the plumes and stronger in the comparatively stagnant regions. This separation of the convecting region into zones of convection and zones of strong magnetic field has been observed in models of magnetoconvection (Weiss *et al.* 1996; Tao *et al.* 1998).

6.1. *Taylor's constraint*

The velocity field in both the moderate and low Ekman number cases shows no evidence of a substantial mean flow ($l = m = 0$ component) developing. Since the saturated field is large, the Elsasser number and hence the Lorentz force are strong in these solutions. From (2.8), (2.12a) and the boundary condition on f, (2.18), we obtain

$$\int_{-1/2}^{1/2} [E\nabla^2\omega_z + \hat{\boldsymbol{z}} \cdot \nabla \times (\boldsymbol{j} \times \boldsymbol{B})]\, \mathrm{d}z = 0. \tag{6.1}$$

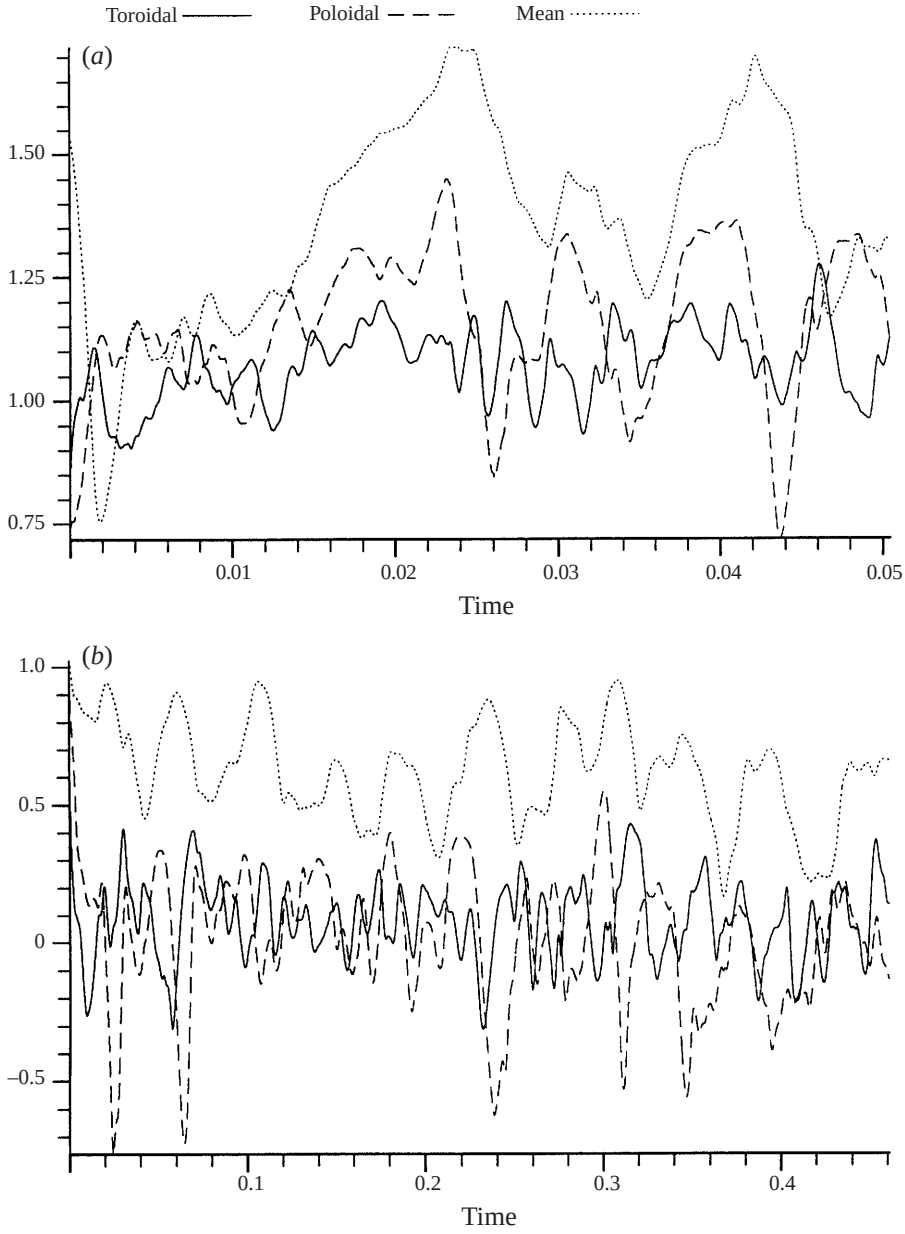

FIGURE 14. As for figure 6: (*a*) Run B ($Ra = 500$, $q = 5$, $E = 0.0002$, $\alpha = \beta = 2\pi$); (*b*) Run D ($Ra = 500$, $q = 1$, $E = 0.0002$, $\alpha = \beta = 2\pi$).

Taylor (1963) suggested (for the spherical problem) that at low E the magnetic field would satisfy a constraint, which for our Cartesian geometry is

$$\int_{-1/2}^{1/2} \hat{\boldsymbol{z}} \cdot \nabla \times (\boldsymbol{j} \times \boldsymbol{B}) \, \mathrm{d}z = 0, \tag{6.2}$$

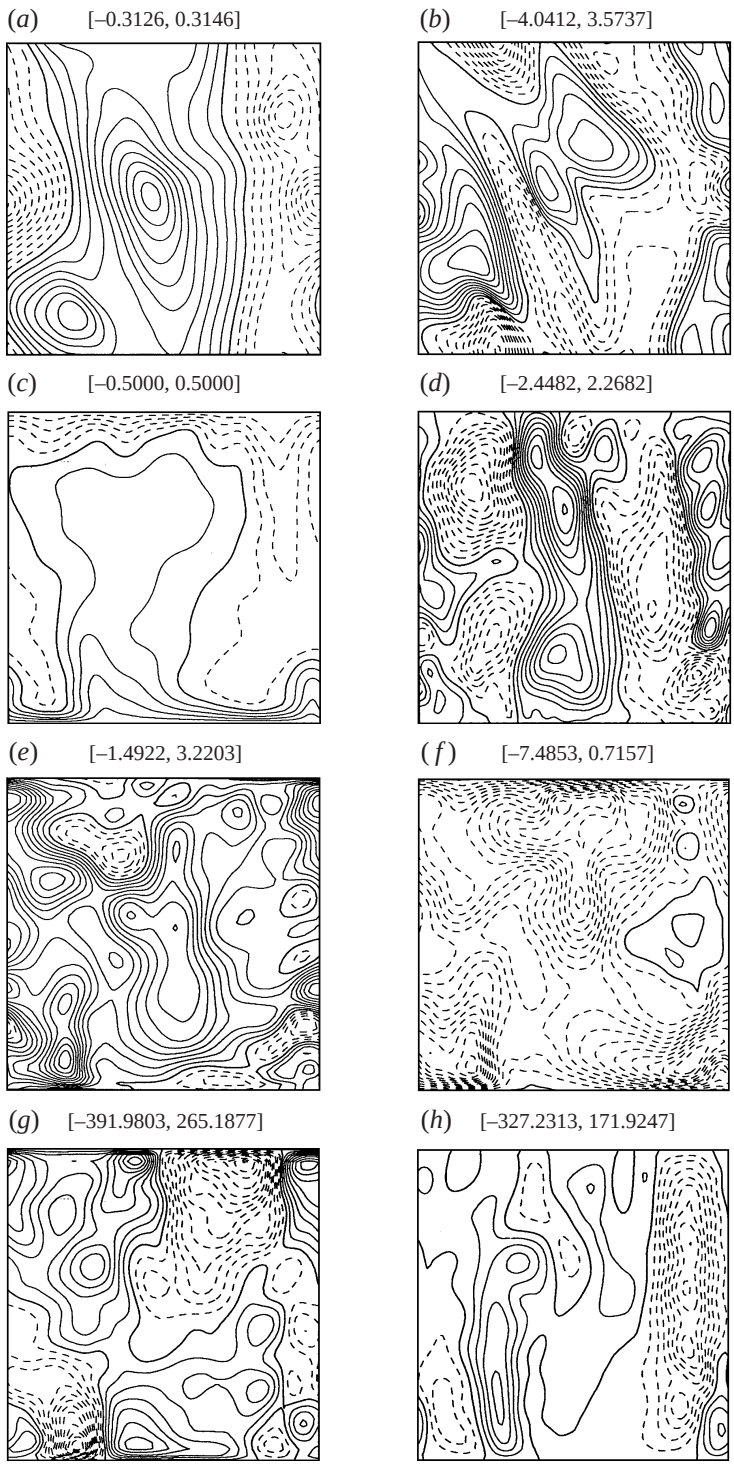

FIGURE 15. A snapshot of magnetic field for the case $Ra = 500$, $E = 0.0002$, $q = 1$, $\alpha = \beta = 2\pi$ (Run D). (*a*) Temperature at intervals of 0.03 in the (x, y)-plane $z = 0.25$. (*b*) B_z at intervals of 0.4 in the (x, y)-plane $z = 0.25$. (*c*) Temperature at intervals of 0.1 in the (x, z)-plane. (*d*) B_z at intervals of 0.25 in the (x, z)-plane. (*e*) B_x at intervals of 0.3 in the (x, z)-plane. (*f*) B_y at intervals of 0.6 in the (x, z)-plane. (*g*) u_x at intervals of 30.0 in the (x, z)-plane. (*h*) u_z at intervals of 40.0 in the (x, z)-plane.

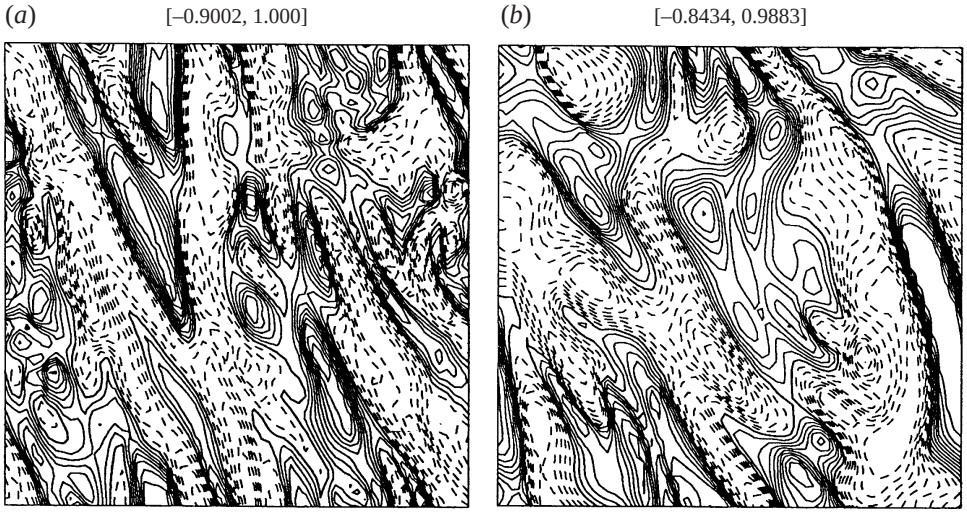

FIGURE 16. Taylor's constraint plots in the (x, y) plane for $Ra = 500$, $q = 1$; (*a*) $E = 0.001$, (*b*) $E = 0.0002$.

to hold at every value of x and y. Note that this is a stronger constraint than in the spherical case, where the integral over the Taylor cylinder must be zero for every value of s, the distance from the rotation axis (e.g. see Jones 1991). The fact that the constraint holds over a plane rather than a line is a consequence of the fact that every curve in the (x, y)-plane is a geostrophic contour in our geometry.

The question of whether Taylor's constraint is satisfied in dynamic dynamos as $E \to 0$ is still controversial: if small-scale features do not appear in the flow, and the magnetic field remains at $O(1)$ strength, the constraint must be satisfied. If the only small-scale features are the Ekman layers, then in the limit $E \to 0$ the Ekman term in (6.1) becomes $O(E^{1/2})$ (see e.g. Fearn 1994) and so either the field remains at $O(1)$ strength and satisfies Taylor's constraint or it reduces to $O(E^{1/4})$ strength and need not satisfy (6.2): the latter case is known as an Ekman state solution.

To obtain a meaningful plot of whether Taylor's constraint is satisfied or not, we plot in figure 16

$$\int_{-1/2}^{1/2} \hat{\boldsymbol{z}} \cdot \nabla \times (\boldsymbol{j} \times \boldsymbol{B})\, \mathrm{d}z \Bigg/ \int_{-1/2}^{1/2} \hat{\boldsymbol{z}} \cdot |\nabla \times (\boldsymbol{j} \times \boldsymbol{B})|\, \mathrm{d}z, \tag{6.3}$$

which is a measure of the degree to which 'Taylorization' has occurred (Anufriev, Cupal & Hejda 1995). Taylor's constraint should be satisfied not by the field becoming small, but by negative and positive contributions to the z-integral cancelling in the numerator of (6.2). Otherwise, magnetic field becomes small as E decreases, an undesirable feature for a geodynamo model.

Figures 16(*a*) and 16(*b*) are for $E = 10^{-3}$ and 2×10^{-4}, respectively. Surprisingly, there is no very clear evidence of Taylorization; the average values of the modulus of the quantity plotted is about 0.3 in both cases. These figures are of course for a snapshot in time, but there is no evidence to suggest these figures are untypical. The low-order Fourier modes do however satisfy Taylor's constraint: the horizontal averages corresponding to figures 16(*a*) and 16(*b*) are close to zero; the small lengthscales apparent in the figures suggested that the low-order harmonics might also be small and

this was indeed confirmed. In consequence, it appears that Taylor's constraint is satisfied in a progressive manner as $E \to 0$. As E gets smaller, finer-scale field structures arise, induced by the small-scale velocity field. Although Taylor's constraint is satisfied for fields with wavenumbers up to some viscous limit l_v, there will always be a range of wavenumbers $l > l_v$ for which Taylor's constraint does not hold. In consequence, it is not clear that (6.3) will ever tend to zero uniformly in the limit $E \to 0$, even though the large-scale components of the field are clearly satisfying Taylor's constraint.

7. Conclusions

Although the nonlinear plane layer dynamo is a difficult problem, it offers a good hope for understanding fundamental dynamo processes. The computing resources required for this problem are considerably less than those required for the spherical problem; nevertheless, they are very substantial. To get to low Ekman number the resolution must be increased and the timestep reduced, substantially increasing the cost of the computation. It should be noted that here we have got well resolved results at comparatively low truncation compared to some studies of non-rotating (or slowly rotating) convection-driven dynamos, but this is a consequence of the parameter regime we are working in, and the magnetic boundary conditions applied. The dynamo we have found is quite efficient, in that it can operate at moderate magnetic Reynolds numbers which is why we have been able to perform long runs and study the mechanism in some detail. As computers increase in speed, it should become possible to explore some of the more difficult areas of parameter space, such as lower values of E. The plane layer problem is a valuable testbed on which to develop new numerical techniques and to explore the dynamics of nonlinear dynamos.

The nature of the non-magnetic convection problem has been shown to have an important influence on the dynamo process. The non-magnetic convection problem is far from being completely understood; in this investigation a wealth of different dynamical behaviour was found, which needs systematic analysis. Only those regimes found in the particular parameter values we considered have been explored in detail, and it is likely that this is a very rich problem.

The existence of dynamo action in these models has been well-established, as has subcritical behaviour. The kinematic dynamo problem behaves in a way broadly similar to that found in fast dynamo investigations, but an encouraging feature is that the saturated magnetic regime behaved in a somewhat more easily understood fashion, at least in the parameter regime investigated here. The mechanism of field generation has been examined and a simplified model proposed, which could be further developed. The Küppers–Lortz instability leading to the rotation of the convection pattern, together with the key role played by the mean field are important features here.

A start has been made on the problem of the low Ekman number dynamo problem, without the use of artificial assumptions such as hyperdiffusion. Much remains to be done in this area, but the suggestion from these numerical experiments is that the convecting region may divide into regions where the mean field dominates and little convection occurs, and comparatively thin regions where viscously controlled plumes carry the heat flux. If confirmed, this is an attractive picture capable of further modelling.

We thank A. M. Soward, S. Childress and A. D. Gilbert for helpful discussions. P.H.R. was supported by a PPARC visiting fellowship GR/K97493. The computing

was performed on machines purchased through the PPARC grant GR/K06495. We also acknowledge support from the NSF grant EAR97-25627.

Appendix. Numerical methods

Three-dimensional nonlinear MHD calculations require significant computational resources, so the choice of numerical method is quite critical. The choice will also depend on the machine architecture; the code used here was implemented on fast but non-parallel workstations. The general techniques used here are not original, but there are a number of different ways of implementing these techniques. The procedure is therefore outlined so that its performance may be compared with that of other methods.

We expand the scalar e appearing in (2.6) as

$$e = \sum_{l=-N_x+1}^{N_x} \sum_{m=-N_y+1}^{N_y} \sum_{n=1}^{N_z+2} e_{lmn} \exp \mathrm{i}(l\alpha x + m\beta y) T_{n-1}(2z). \tag{A 1}$$

Similar expansions are used for g, h and θ, but the expansion for f over z goes up to $N_z + 4$ to accommodate the four boundary conditions satisfied by f at $z = \pm\frac{1}{2}$. Not all the complex e_{lmn} are independent, because the reality conditions, typically

$$e_{l,m,n} = \bar{e}_{-l,-m,n} \tag{A 2}$$

must hold. The independent components for e–h are then

$$1 \leqslant l \leqslant N_x, -N_y + 1 \leqslant m \leqslant N_y, \quad \text{and} \quad l = 0, 1 \leqslant m \leqslant N_y, \tag{A 3}$$

the $l = m = 0$ modes being replaced by the mean quantities U_x, U_y, b_x and b_y which are expanded over z only. The θ expansion has independent components

$$1 \leqslant l \leqslant N_x, -N_y + 1 \leqslant m \leqslant N_y, \quad \text{and} \quad l = 0, 0 \leqslant m \leqslant N_y. \tag{A 4}$$

At each timestep, the momentum equations (2.8), (2.9), (2.14) and (2.15) are solved first. The discrete equations are obtained by collocation at the N_z zeros of $T_{N_z}(2z)$ for each independent mode (l, m) of (A 3) and (A 4). The nonlinear Lorentz force terms are evaluated by calculating $\boldsymbol{j}$ and $\boldsymbol{B}$ in spectral space from the expansions of g and h, and converting these six quantities to real space, i.e. evaluating them on the z-collocation points and a $2N_x \times 2N_y$ regular grid in $x - y$ space. The vector product $\boldsymbol{j} \times \boldsymbol{B}$ is then found on the mesh, and the resulting three components are converted back to spectral space. The z-components of the curl and curl curl of the Lorentz force (together with the appropriate mean values) are the quantities required to solve (2.8), (2.9), (2.14) and (2.15).

The linear terms in both the momentum equations and the other equations are handled by pre-computing the inverse of the matrices derived from the diffusion operator; this has the slight disadvantage that this is an order-N^4 process (assuming N_x, N_y and N_z are all $O(N)$), while the computation of the transforms of the nonlinear terms is only $O(N^3 \log N)$. Nevertheless, because of the complexity of the nonlinear terms, the time spent in computing the linear terms was small compared to that computing the nonlinear terms. An alternative would be to differentiate (and integrate) the Chebyshev expansions at each timestep, only an $O(N_z)$ operation per horizontal mode; however, because of the high order of the system a large number of differentiations are required, so that this will only become efficient at large N_z. A more pressing reason for adopting the alternative method is likely to

be storage considerations; the pre-computed matrices are $O(N^4)$ and their size will create difficulty at large N_z.

Once the momentum equations have been solved, we can feed in the velocities to advance the induction and temperature equations to the next timestep. The nonlinear terms in these equations are handled similarly to those in the momentum equation; since $\boldsymbol{B}$ has already been computed on the mesh, a significant saving is possible here. The equations are advanced using second-order Crank–Nicolson for the diffusion terms; the nonlinear terms are handled explicitly. A predictor-corrector scheme was used; the predictor advances the solution using a first-order Euler step for the nonlinear terms; these nonlinear terms are then averaged between the original and predicted values, and then a second-order corrector step is taken. This allows the timestep to be controlled as the integration proceeds. This seems to be important for this problem, as 'difficult' time intervals occur during which the timestep has to be significantly lower than its average value.

The most time consuming operation is the conversion of the components of $\boldsymbol{j}$, $\boldsymbol{B}$ and $\boldsymbol{u}$ from spectral space to the mesh and the conversion of the nonlinear terms back to spectral space. Standard FFT routines are optimized for large N transforms; here we have to do comparatively short transforms (typically $N = 24, 32, 48$ and 64) many times. Significant savings were obtained using purpose built transforms for these lengths.

The appropriate truncation level for our parameter regime was determined by integrating the equations forward for a comparatively short time (typically a thousand timesteps) at different resolutions. Resolution was judged adequate when the results differed from higher truncations by less than 1%. It should be noted that because our solutions are all chaotic, long time runs at different resolution will inevitably differ considerably, because the solution at large time is sensitive to initial conditions. Nevertheless, the hope is that the general behaviour will not be affected.

As E is reduced, the timestep as determined by our automatic procedure is reduced approximately proportionally as suggested by Walker *et al.* (1998). This is a consequence of our explicit treatment of the nonlinear terms. This is a strong limitation on reducing the value of E; not only does the number of modes need to be increased, but the number of steps per diffusion time required rises also, unfortunately making it impractical to go much below $E = 10^{-4}$.

REFERENCES

Anufriev, A. P., Cupal, I. & Hejda, P. 1995 The weak Taylor state in an $\alpha\omega$–dynamo. *Geophys. Astrophys. Fluid Dyn.* **79**, 125–145.

Braginsky, S. I. 1975 Nearly axisymmetric model of the hydromagnetic dynamo of the Earth I. *Geomagn. & Aeron.* **15**, 122–128.

Brandenburg, A., Jennings, R. L., Nordlund, Å., Rieutord, M., Stein, R. F. & Tuominen, I. 1996 Magnetic structures in a dynamo simulation. *J. Fluid Mech.* **306**, 325–352.

Brummell, N. H., Cattaneo, F. H. & Tobias, S. M. 1998 Linear and nonlinear dynamo action. *Phys. Lett.* **249**, 437–442.

Busse, F. H. & Heikes, K. E. 1980 Convection in a rotating layer: a simple case of turbulence. *Science* **208**, 173.

Chandrasekhar, S. 1961 *Hydrodynamic and Hydromagnetic Stability*. Clarendon.

Childress, S. & Soward, A. M. 1972 Convection driven hydromagnetic dynamo. *Phys. Rev. Lett.* **29**, 837–839.

Childress, S. & Gilbert, A. D. 1995 *Stretch, Twist, Fold: the Fast Dynamo*. Springer.

Fautrelle, Y. & Childress, S. 1982 Convective dynamos with intermediate and strong fields. *Geophys. Astrophys. Fluid Dyn.* **22**, 235–279.

Fearn, D. R. 1994 Nonlinear planetary dynamos. In *Stellar and Planetary Dynamos* (ed. M. R. E. Proctor & A. D. Gilbert), pp. 219–244. Cambridge University Press.

Gilbert, A. D. & Sulem, P.-L. 1990 On inverse cascades in alpha effect dynamos. *Geophys. Astrophys. Fluid Dyn.* **51**, 243–261.

Glatzmaier, G. A. & Roberts, P. H. 1995*a* A three-dimensional convective dynamo solution with rotating and finitely conducting inner core and mantle. *Phys. Earth Planet. Inter.* **91**, 63–75.

Glatzmaier, G. A. & Roberts, P. H. 1995*b* A three-dimensional self-consistent simulation of a geomagnetic field reversal. *Nature* **377**, 203–209.

Gog, J. R., Oprea, I., Proctor, M. R. E. & Rucklidge, A. M. 1999 Destabilization by noise of tranverse perturbations to heteroclinic cycles: a simple model and an example from dynamo theory. *Proc. R. Soc. Lond.* (in press).

Jones, C. A. 1991 Dynamo models and Taylor's constraint. In *Advances in Solar System Magneto-hydrodynamics* (ed. E. R. Priest & A. W. Hood), pp. 25–50. Cambridge University Press.

Jones, C. A. & Roberts, P. H. 1990 Magnetoconvection in rapidly rotating Boussinesq and compressible fluids. *Geophys. Astrophys. Fluid Dyn.* **55**, 263–308.

Jones, C. A., Longbottom, A. W. & Hollerbach, R. 1995 A self-consistent convection driven geodynamo model, using a mean field approximation. *Phys. Earth Planet. Inter.* **92**, 119–144.

Küppers, G. & Lortz, D. 1969 Transition from laminar convection to thermal turbulence in a rotating fluid layer. *J. Fluid Mech.* **35**, 609–620.

Matthews, P. C. 1999 Dynamo action in simple convective flows. *Proc. R. Soc. Lond.* A **455**, 1829–1840.

Meneguzzi, M. & Pouquet, A. 1989 Turbulent dynamos driven by convection. *J. Fluid Mech.* **205**, 319–340.

Roberts, P. H. & Jones, C. A. 1999 The onset of magnetoconvection at large Prandtl number in a rotating layer I. Finite magnetic diffusion. *Geophys. Astrophys. Fluid Dyn.* (submitted).

Soward, A. M. 1974 A convection driven dynamo I. The weak field case. *Phil. Trans. R. Soc. Lond.* A **275**, 611–651.

Soward, A. M. 1984 Bifurcations and stability of finite amplitude convection in a rotating layer. *Physica* D **14**, 227–241.

Soward, A. M. & Jones, C. A. 1983 α^2-dynamos and Taylor's constraint. *Geophys. Astrophys. Fluid Dyn.* **27**, 87–122.

St-Pierre, M. 1994 The strong field branch of the Childress–Soward dynamo. In *Stellar and Planetary Dynamos* (ed. M. R. E. Proctor & A. D. Gilbert), pp. 295–302. Cambridge University Press.

Tao, L., Weiss, N. O., Brownjohn, D. P. & Proctor, M. R. E. 1998 Flux separation in stellar magnetoconvection. *Astrophys. J.* **496**, L39–44.

Taylor, J. B. 1963 The magnetohydrodynamics of a rotating fluid and the Earth's dynamo problem. *Proc. R. Soc. Lond.* A **274**, 274–283.

Walker, M. R., Barenghi, C. F. & Jones, C. A. 1998 A note on dynamo action at asymptotically small Ekman number. *Geophys. Astrophys. Fluid Dyn.* **88**, 261–275.

Weiss, N. O., Brownjohn, D. P., Matthews, P. C. & Proctor, M. R. E. 1996 Photospheric convection in strong magnetic fields. *Mon. Not. R. Astron. Soc.* **283**, 1153–1164.

Zhang, K. & Jones, C. A. 1997 The effect of hyperviscosity on geodynamo models. *Geophys. Res. Lett.* **24**, 2869–2872.

Zhang, K. & Roberts, P. H. 1997. Thermal inertial waves in a rotating fluid layer: exact and asymptotic solutions. *Phys. Fluids* **9**, 1980–1987.

Zhang, K. & Roberts, P. H. 1998. A note on stabilising and destabilising effects of Ekman boundary layers. *Geophys. Astrophys. Fluid Dyn.* **9**, 1980–1987.